The Description and Validation of a Computationally-Efficient CH_4-CO-OH (ECCOHv1.01) Chemistry Module for 3D Model Applications

Elshorbany, Yasin F.[1,2*], Duncan, Bryan N.[1], Strode, Sarah A.[1,3], Wang, James S.[1,3], Kouatchou, Jules[1,4]

[1]NASA Goddard Space Flight Center, Greenbelt, Maryland, USA
[2]Earth System Science Interdisciplinary Center, University of Maryland, College Park, Maryland, USA
[3]Universities Space Research Association, Columbia, Maryland, USA
[4]Science Systems and Applications Inc., Lanham, Maryland, USA
*Correspondence to: Y. F. Elshorbany (yasin.f.elshorbany@nasa.gov)

Abstract:

We present the Efficient CH_4-CO-OH chemistry module (ECCOH) that allows for the simulation of the methane, carbon monoxide and hydroxyl radical (CH_4-CO-OH) system, within a chemistry climate model, carbon cycle model, or earth system model. The computational efficiency of the module allows many multi-decadal sensitivity simulations of the CH_4-CO-OH system, which primarily determines the global atmospheric oxidizing capacity. This capability is important for capturing the nonlinear feedbacks of the CH_4-CO-OH system and understanding the perturbations to methane, CO and OH and the concomitant impacts on climate. We implemented the ECCOH chemistry module into the NASA GEOS-5 Atmospheric Global Circulation Model (AGCM), performed multiple sensitivity simulations of the CH_4-CO-OH system over two decades, and evaluated the model output with surface and satellite datasets of methane and CO. The favorable comparison of output from the ECCOH chemistry module (as configured in the GEOS-5 AGCM) with observations demonstrates the fidelity of the module for use in scientific research.

1 Introduction

The coupled methane - carbon monoxide - hydroxyl radical (CH_4-CO-OH) system is nonlinear (e.g., Prather, 1994) and important in determining the atmosphere's oxidizing capacity (e.g., Chameides et al., 1976). Methane is the second most important anthropogenic greenhouse gas (GHG), though its 100-year global warming potential (GWP) is 34 times larger than that for carbon dioxide (CO_2; Myhre et al., 2013). Methane is responsible for about 20% of the warming induced by long-lived GHG's since pre-industrial times (Kirschke et al., 2013). The CH_4-CO-OH system has implications for tropospheric ozone and, subsequently, air quality (e.g., Fiore et al., 2002). A thorough understanding of historical methane, CO and OH trends and variations is necessary to credibly predict future changes and their climate feedback, as well as, to develop strategic national and international emission reduction policies.

The major limitation of forward modeling studies of trends and variability in the CH_4-CO-OH system is the computational expense associated with simulating ozone-nitrogen oxides-volatile organic compounds (O_3-NO_x-VOC) photochemistry for the determination of OH, particularly since perturbations to relatively long-lived methane (~8-10 y) can take several

42   decades to fully evolve (e.g., Prather, 1996). There are few forward modeling studies in the
43   literature that carry a full representation of O_3-NO_x-VOC chemistry, and they necessarily
44   present a limited number of sensitivity simulations (e.g., Fiore et al., 2006; Voulgarakis et
45   al., 2015).

46   To overcome this computational expense, global modeling communities often use archived
47   and annually-repeating monthly OH fields to simulate the oxidation of methane and CO. In
48   the TransCom methane model intercomparison project (MIP), archived and annually-
49   repeating OH fields were used from a climatology (Spivakovsky et al., 2000). Wang et al.
50   (2004) used archived and annually-varying OH fields from Duncan et al. (2007a) to explain
51   the causes of observed interannual variations in methane and the observed slowdown in its
52   growth rate from 1988 to 1997.

53   Limitations of using archived, monthly OH fields for studies of methane's and CO's
54   evolution are that feedbacks of the CH_4-CO-OH system on methane, CO and OH are not
55   captured as the losses of methane and CO by reaction with OH are assumed to be linearly
56   proportional to the OH fields. For methane, this assumption is not desirable, particularly on
57   multi-decadal time-scales (e.g., Prather, 1996). Chen and Prinn (2006) found that using an
58   archived, annual cycle of OH may mask or bias the interannual changes of methane. For
59   relatively short-lived CO (~1-2 months), this assumption is not valid given the strong
60   feedback between CO and OH (e.g., Duncan and Logan, 2008; Voulgarakis et al., 2015). If a
61   multi-decadal simulation of methane or CO using archived and annually-repeating OH
62   reproduces observations, then there must be some compensating factor, for example a bias in
63   emissions. That is, the simulation reproduces observations, but for the wrong reason. The
64   models in the TranCom MIP adjusted down (by 8%) the archived OH climatology of
65   Spivakovsky et al. (2000) so that the simulated decline in the global, atmospheric
66   methylchloroform (MCF) concentration since 2000 better matched that observed (Patra et al,
67   2011). Adjusting archived OH to improve a simulation of MCF, methane and/or CO makes
68   the specious assumption that emissions inventories, model dynamics, etc. used in the
69   simulation are correct. If using archived and annually-repeating OH, whether adjusted or
70   not, inverse modeling studies of methane and CO will incorrectly determine a posteriori
71   fluxes as the impact of nonlinear feedbacks of the CH_4-CO-OH system on concentrations
72   will be erroneously folded into the flux estimates. Therefore, there is a need for a
73   computationally-efficient solution to simulate credible temporal and spatial distributions of
74   OH over several decades, while capturing the nonlinear feedbacks of the CH_4-CO-OH
75   system.

76   In this manuscript, we present and validate the new, computationally-<u>E</u>fficient <u>C</u>H<u>4</u>-<u>C</u>O-
77   <u>O</u>H (ECCOH; pronounced like "echo") chemistry module to interactively simulate the
78   chemistry of the CH_4-CO-OH system within a chemistry-climate model, carbon cycle model,
79   or Earth System Model. The computational efficiency of the ECCOH chemistry module
80   allows many sensitivity simulations of multiple decades to be performed, which is important
81   for capturing the nonlinear feedbacks of the CH_4-CO-OH system and understanding the
82   perturbations to methane and the concomitant impacts on climate. The ECCOH chemistry
83   module allows one to deconvolve the impacts of various causal factors (e.g., overhead ozone
84   column, NO_x, VOCs, water vapor, etc.) on OH and, subsequently, on methane and CO.
85   Therefore, this capability is valuable in determining these impacts, especially, given that

86 simulated OH varies widely between models (Shindell et al., 2006; Fiore et al., 2009) for a
87 variety of reasons, including differences in the causal factors that influence OH (Shindell et
88 al., 2006). For instance, Voulgarakis et al. (2013) found that simulated tropospheric methane
89 lifetimes of various models ranged from ~7 to ~14 years; this spread is similar to that
90 calculated by Shindell et al. (2006) and Fiore et al. (2009), even when all participating
91 models used identical methane abundances and CO emissions (Shindell et al., 2006).
92 Shindell et al. (2006) related the wide spread of simulated CO between models to the large
93 spread in simulated OH. Furthermore, simulated OH from full chemistry mechanisms in
94 global models is still highly uncertain because of incomplete knowledge and representation
95 of OH sources, sinks and recycling (e.g., Elshorbany et al., 2010, 2012a, 2012b, 2014; Stone
96 et al., 2012). For example, 1) nitrous acid (HONO) is typically underestimated in models by
97 an order of magnitude (Elshorbany et al., 2012b), which can lead to a significant
98 underestimation of OH, especially in urban high-NO_x regions; 2) in unpolluted, forested
99 environments, significant discrepancies exist between models and measurements (Stone et
100 al., 2012); and 3) Patra et al. (2014) indicate that the inter-hemispheric OH ratio (northern to
101 southern hemisphere) is near unity, while a recent model inter-comparison had a multi-model
102 average of about 1.3.
103 The manuscript is organized as follows: In Sect. 2, we 1) describe the ECCOH chemistry
104 module as implemented in the NASA Goddard Earth Observing System, Version 5
105 Atmospheric General Circulation Model (GEOS-5 AGCM), and 2) and describe a series of
106 simulations, which we refer to as "scenarios" hereafter, to illustrate the utility of the ECOOH
107 module for understanding the influence of various factors on the observed spatial
108 distributions and temporal evolution of methane, CO, and OH. In Sect. 3, we show that the
109 simulated trends and variations of methane and CO in our reference scenario agree well with
110 in situ and satellite measurements. In Sect. 4, we demonstrate the ability of the ECCOH
111 chemistry module to capture the nonlinear chemistry of the CH_4-CO-OH system with output
112 from our sensitivity scenarios.

113 2 Technical Approach and Methodology

114 2.1 Description of the ECCOH Chemistry Module and Its Implementation

115 The ECCOH chemistry module is composed of a parameterization of tropospheric OH and
116 tracers of methane and CO as shown in Fig. 1. The advantage of the ECCOH chemistry
117 module over a full representation of O_3-NO_x-VOC chemistry is computational
118 efficiency. The computational cost of simulating tropospheric OH is reduced by about a
119 factor of 500 when the full O_3-NO_x-VOC chemistry is replaced by the parameterization of
120 OH (Duncan et al., 2000). This computationally-efficient parameterization of OH allows 1)
121 for many multi-decadal model sensitivity simulations to be performed and 2) one to
122 deconvolve the impact of various factors on the observed trends and variability in methane
123 and CO. It is based on the method described by Spivakovsky et al. (1990a), who developed
124 an earlier version of the parameterization of OH used in several studies, including
125 Spivakovsky et al. (1990b) and Prather and Spivakovsky (1990). The parameterization of
126 OH of Duncan et al. (2000) is designed to simulate OH over the range of photochemical
127 environments found throughout the troposphere, including a wide enough range so as to be

128   applicable to preindustrial, present day and possible future conditions (Duncan et al., 2000).
129   It has been implemented into two host atmospheric models and has been used in several
130   studies of the nonlinear feedbacks of CO and OH (Duncan et al., 2007a; Duncan and Logan,
131   2008; Strode et al., 2015).

132   The parameterization of OH accurately represents OH predicted by a full chemical
133   mechanism as a set of high-order polynomials that describe the functional relationship
134   between the concentration of OH and meteorological variables (i.e., pressure, temperature,
135   cloud albedo), solar irradiance variables (i.e., ozone column, surface albedo, declination
136   angle, latitude) and chemical variables, including CO and methane as well as nitrogen oxides
137   (as a family), ozone, water vapor, and various VOCs. That is, the 24-hour average OH is
138   calculated interactively in the model and responds to changes in the concentrations of trace
139   gases and meteorology. Input variables to the parameterization of OH may be taken from
140   archived fields from, for instance, an observational climatology or archived fields from a
141   model simulation with a full representation of trace gas and aerosol atmospheric chemistry,
142   and may be annually-repeating or annually-varying. Some variables (e.g., water vapor,
143   clouds) may be taken from the host model as the simulation progresses. Ideally, all input
144   variables should be annually-varying so as to best capture the nonlinear feedbacks of the
145   CH_4-CO-OH system. If one chooses to use output from a single computationally-expensive
146   full chemistry model simulation as input to the parameterization of OH, subsequent
147   sensitivity simulations using the ECCOH chemistry module will be far less computationally-
148   expensive relative to that single expensive simulation, which is the primary strength of using
149   the parameterization of OH. In Section 2.2, we discuss the setup of the simulations presented
150   in this study.

151   We adjust the OH from the parameterization to account for important updates in kinetic
152   information of O^1D reactions by water vapor, molecular nitrogen, and molecular oxygen
153   (Sander et al., 2011). These reactions are key as the primary production pathway (P) for OH
154   involves the formation of excited O^1D atoms by photolysis of ozone (O_3), followed by their
155   reaction with water vapor in competition with their collisional quenching by molecular
156   nitrogen and oxygen: P = $j[O_3]$ * $2k_1[H_2O]$ / ($k_1[H_2O]$ + $k_2[N_2]$ + $k_3[O_2]$), where j is the
157   ozone photolysis rate and k_1, k_2 and k_3 are the rate constants of O^1D reactions with water
158   vapor, nitrogen and oxygen, respectively. Typically, this adjustment decreases OH by 10-
159   30%, depending on altitude and season. Recent updates in isoprene chemistry are not
160   reflected in the parameterization of OH, so OH near the surface in clean, forested
161   environments (e.g., Amazon and Congo basins) is too low relative to current knowledge
162   (e.g., Fuchs et al., 2013). However, the contribution of these regions to global methane and
163   CO loss is small (i.e., < 1%) and the current knowledge of isoprene photochemistry is still
164   highly uncertain (Fuchs et al., 2013). Ultimately, the parameterization of OH reflects
165   uncertainties in the chemistry upon which it is based, as do the photochemical mechanisms
166   in all atmospheric chemistry models (e.g., Stone et al., 2012; Fuchs et al., 2013). The losses
167   of methane and CO in the ECCOH chemistry module are determined by their reaction with
168   tropospheric OH. Additional losses of methane in the stratosphere occur by reactions with
169   OH, Cl and O^1D, whose distributions are simulated using archived and annually-repeating
170   monthly fields.

171   We implemented the ECCOH chemistry module into the Goddard Earth Observing

172 System, Version 5 Atmospheric General Circulation Model (GEOS-5 AGCM, Fortuna
173 version, Rienecker et al., 2008; Pawson et al., 2008; Ott et al., 2010; Molod et al., 2012).
174 The AGCM combines the finite volume dynamical core described by Lin (2004) with the
175 GEOS-5 column physics package, as summarized by Rienecker et al. (2008). The AGCM
176 domain extends from the surface to 0.01 mb and uses 72 hybrid layers that transition from
177 terrain following near the surface to pure pressure levels above 180 mb. We use a horizontal
178 resolution of 2° latitude × 2.5° longitude and the time step is 30 minutes for physical
179 computations.

2.2 Description of the Reference and Sensitivity Scenarios

181 To demonstrate the utility of the ECCOH chemistry module for multi-decadal studies, we
182 performed several model simulations using the module in the GEOS-5 AGCM (Table 1 and
183 Table 2). The model setup (i.e., emissions, input to the parameterization of OH, and
184 dynamics) of the reference scenario, which we refer to as the *Base* scenario, is detailed in
185 Table 1. Compared to the sensitivity scenarios described in Table 2, the *Base* scenario is the
186 least complex. For example, all CO emissions and natural methane emissions are for one
187 year that are repeated for each year of the simulation (1988-2007); therefore, interannual
188 variations in methane and CO levels caused by variations in these emissions will not be
189 captured in the *Base* scenario. However, there are two important sources of variability that
190 are included in the *Base* scenario. First, the dynamics are constrained by varying sea surface
191 temperatures and sea ice concentrations. Therefore, the *Base* scenario will capture variations
192 in methane, CO, and OH resulting from meteorological variations, such as those associated
193 with the El Niño Southern Oscillation (ENSO). In addition, atmospheric temperature,
194 pressure and specific humidity are calculated online by the GEOS-5 AGCM and are fed into
195 the parameterization of OH as the runs progress, so interannual variations in water vapor,
196 temperature, and cloud cover are also included in the *Base* scenario. These factors are known
197 to influence variations in OH and thus CO and methane (e.g., Holmes et al., 2013). Second,
198 interannual variations in anthropogenic methane sources are included in the *Base* scenario. In
199 Sect. 3, we evaluate model output from the *Base* scenario with the observational datasets
200 described in Table 3.
201 We present the results of our sensitivity scenarios in Sect. 4. We explore the influence of
202 several causal factors on the observed spatial distributions and temporal evolutions of
203 methane, CO, and OH. These causal factors include annually-varying methane and CO
204 emissions (i.e., Scenarios 2-4 in Table 2; natural methane emissions, and anthropogenic and
205 natural CO emissions, Figs. S1 and S2 in the Supplement) and annually-varying input
206 variables to the parameterization of OH (i.e., Scenario 5 in Table 2).

3 Evaluation of the *Base* Scenario

208 We evaluate the model output of methane and CO from the *Base* scenario with satellite
209 and in situ observations (Table 3). We also compare simulated OH with that from a GEOS-5
210 AGCM simulation (with a full representation of O_3-NO_x-VOC chemistry (Strode et al.,
211 2015)). We highlight where the *Base* scenario's simplicity results in a poor or satisfactory
212 comparison of the model output with the observed temporal and spatial distributions of

methane, CO, and OH. We demonstrate that the ECCOH chemistry module for this scenario reasonably captures the distributions of methane and CO, within the limitations of this scenario, as compared to measurements and other model studies (e.g., Shindell et al. 2006; Patra et al., 2011; Naik et al., 2013).

3.1 Tropospheric OH

There are very few direct observations of OH with which to constrain models (e.g., Stone et al., 2012) and none on regional or global scales. Therefore, the MCF lifetime inferred from measurements serves as a widely used, indirect proxy for global OH abundance (e.g., Lawrence et al., 2001). Though useful, the MCF lifetime gives an incomplete description of the spatial and vertical distributions of OH (e.g., Lawrence et al., 2001) and there are uncertainties concerning MCF emissions and the resulting lifetime estimate (e.g., Wang et al., 2008). Nevertheless, the MCF data have been recently used to infer the ratio of OH in the Northern to the Southern Hemisphere (Patra et al., 2014).

Despite the challenges concerning OH, we show in this section that the spatial and vertical distributions of simulated global mean OH (Fig. 2 and Fig. 3) from the *Base* scenario are reasonable relative to the MCF proxy for OH as well as to simulated OH from other models. Related to the OH dependency on UV radiation (Rohrer and Berresheim, 2006), the maximum and minimum OH levels at any given location occur in local summer and winter, respectively (Fig. 2). OH maximizes around 600 mb because of vertical dependencies of the main sources and sinks of OH (Spivakovsky et al., 1990). The seasonal and vertical distributions of the zonal mean OH in the *Base* scenario are comparable to the OH climatology of Spivakovsky et al. (2000; see Figure 6 of Spivakovsky et al.), despite the different inputs given to the parameterization of OH in the two studies.

The interannual variations in global OH (given by the annual mean standard deviation, not shown) are small (<5%) and mainly related to meteorological variations (e.g., water vapor, clouds, temperature, and transport) as annually-repeating emissions are used in the *Base* scenario, except for anthropogenic methane emissions (Table 1, Fig. S 1, Fig. S 2). This result is consistent with Voulgarakis et al. (2013) who show that OH has the strongest relationship with changes in temperature and humidity when emissions do not vary interannually. As discussed in Sect. 4, we see considerably larger variations in OH in several of our more complex sensitivity simulations, which have interannual variations in methane and CO emissions as well as in factors that affect OH.

Over our simulation period, the range of annual mean, atmospheric MCF lifetimes is 6.08 ± 0.60 to 6.53 ± 0.65 years with respect to loss by reaction with tropospheric OH for the *Base* scenario, assuming a MCF uniform mixing ratio. Our lifetimes are similar to values reported in the literature (e.g., $6.0^{+0.5}_{-0.4}$ years (Prinn et al., 2005); multi-model mean of 5.7 ± 0.9 years (Naik et al., 2013); 6.3 ± 0.9 years (Prather et al., 2012)). The global, annual mean lifetime of methane with respect to tropospheric OH ranges from 10.10 ± 1.06 to 10.86 ± 1.15 years. These values are similar to those inferred from measurements (e.g., $10.2^{+0.9}_{-0.7}$ years (Prinn et al., 2005)) as well as to those reported in previous multi-model comparison studies (e.g., 9.7 ± 1.7 years (Shindell et al., 2006); 10.19 ± 1.72 years (Fiore et al., 2009); 9.7 ± 1.5 years (Naik et al., 2013)). The lifetime of methane is calculated by dividing

255 the total atmospheric burden by the tropospheric methane loss rate (e.g., Fiore et al., 2009).

256 We also compare our simulated OH with that from a GEOS-5 AGCM simulation that

257 carries a full representation of O_3-NO_x-VOC chemistry. This simulation was included in the

258 Atmospheric Chemistry and Climate Model Intercomparison Project (ACCMIP, Lamarque et

259 al., 2013; the model is designated as "GEOSCCM"). Henceforth, we refer to this simulation

260 as the "ACCMIP simulation". The same CO emissions (annually-repeating emissions for

261 year 2000) are used in both the *Base* and ACCMIP simulations, but there are differences

262 between the simulations (e.g., model dynamics, prescribed methane, etc.). Despite these

263 differences, we find that the spatial and vertical distributions of OH are quite similar with

264 differences generally less than 10% (Fig. S 17). The global, mean tropospheric OH in the

265 *Base* scenario of 10.9×10^5 molecules cm^{-3} also compares well with that of 11.4×10^5

266 molecules cm^{-3} from the ACCMIP simulation (the 2000 time slice) as well as within the

267 range of means from other models (e.g., $6.5 - 13.4 \times 10^5$ molecules cm^{-3} (Voulgarakis et al.,

268 2013)).

3.2 Methane

270 *GMD surface data*: We evaluate our simulated surface distributions of methane with data

271 from the NOAA Global Monitoring Division (GMD) network. The simulated, interannual

272 variation of methane's global growth rate agrees reasonably well ($R^2 = 0.44$) with that

273 estimated from GMD data, using all available data from 92 stations over the simulation

274 period 1988-2007 (Fig. 4a). The agreement of model output with observations is worse (R^2

275 $= 0.33$) when we only use the 17 stations that cover the entire simulation period (Fig. 4b).

276 We decided to include all 92 stations, even those without records that cover the entire

277 simulation period, as we are able to nearly reproduce Fig. 4a using 46 stations that have at

278 least 75% data coverage (not shown). A relatively high correlation coefficient ($R^2 = 0.44$)

279 implies that interannual variations in anthropogenic methane emissions and dynamics

280 explain much of methane's growth rate over the study period, which is consistent with the

281 findings of the TransCom MIP (Patra et al., 2011).

282 Overall, the comparison of model output and data at individual GMD stations is favorable.

283 Fig. 5 to Fig. 7 show comparisons for monthly averages, seasonal averages, and annual

284 differences, respectively, at six GMD stations, which were chosen as they have long time

285 records and cover a wide range of latitudes. Over the simulation period (1988-2007), the

286 correlation slope (S) and coefficient (R^2) for these six stations (Table 4) range from 0.56 to

287 0.79 and from 0.58 to 0.91, respectively.

288 There are two important features of the observations that are not simulated in the *Base*

289 scenario. First, the *Base* scenario overestimates methane concentrations by 20-30 ppbv at

290 the northern high latitude stations of Alert and Barrow during the 1980s and 1990s (Fig. 5-

291 Fig. 7). The overestimation of methane in the northern hemisphere during the 1990s occurs

292 because of regional high biases in natural methane emissions (Fig. S 1 and Patra et al., 2011).

293 As shown in Sect. 4.3, simulated methane improves significantly in the northern hemisphere

294 in the $E_{CH4}Vary$ scenario, which includes annually-varying natural methane emissions.

295 Second, the *Base* scenario captures the increasing observed methane trend in the 1990s, but

296 under-predicts methane in the 2000's (Fig. 7). Both of these features (i.e., high bias at high

297 northern latitudes in the 1990's and low bias in the 2000's) are consistent with the findings
298 of the TransCom MIP that used the same methane emissions (Table 1 and Patra et al., 2011).
299 *SCIAMACHY methane*: We compare the simulated methane dry columns to those from
300 SCIAMACHY (Table 3, Fig. 8). The data have the best global spatial coverage during boreal
301 summer because of lower cloud cover during this season (Schneising et al., 2011). The
302 observed methane dry columns reach their highest levels during boreal summer and fall,
303 maximizing over Asia (eastern China and northern India) because of high emissions from
304 wetlands and rice paddies. The *Base* scenario reproduces the spatial distribution of the data
305 well with a bias of < 2% over most of the globe, except over eastern Asia and western US
306 during boreal summer where it is biased low, but still within the measurement uncertainties
307 (~7-10%; Gloudemans et al., 2008; Houweling et al., 2014). Houweling et al. (2014)
308 demonstrate that SCIAMACHY data have a seasonal bias that ranges from about -50 ppb
309 during boreal winter to about +50 ppb during boreal summer as compared to the Total
310 Carbon Column Observing Network (TCCON) measurements, which may also explain the
311 simulated seasonal biases (Fig. 8).

312   3.3   CO

313 *GMD surface data*: The *Base* scenario captures the monthly variability of GMD CO data
314 well with a mean correlations slope (S) and coefficient (R^2) of 0.81 and 0.72, respectively
315 (Fig. 9 to Fig. 11, Table 4). This result indicates that the seasonal CO cycle is well captured
316 in the *Base* scenario (Fig. 11), which includes annually-repeating, but seasonally-varying
317 biomass burning emissions (Fig. S 2). As expected, the *Base* scenario does not capture the
318 significant interannual variations associated with strong variations in emissions (Fig. 9, Fig.
319 10). The low biases reach ~40 ppb in boreal winter and spring at high northern latitudes.
320 During the 1980's and 1990's, CO levels in the northern hemisphere declined substantially
321 because of changing patterns of emissions (Duncan et al., 2007a), which is not simulated
322 with annually-repeating CO emissions. These results are in agreement with the findings of
323 the multi-model ACCENT study (using annually-repeating CO emissions), in which there
324 was a low bias of ~50 ppbv at northern hemisphere high latitude stations (Shindell et al.,
325 2006), as well as with other recent studies (e.g., Monks et al., 2015).
326 *MOPITT and TES/MLS CO:* The primary advantage of satellite data, above ground-based
327 networks, is spatial coverage, so we compare the spatial and seasonal distributions of
328 simulated CO with those from the MOPITT and TES/MLS instruments (Fig. 12, Fig. 13).
329 The distributions of CO from the *Base* scenario compare well overall with the data. The
330 mean biases relative to both datasets are within ±10% over most of the globe and in all
331 seasons. For example, the seasonal correlation slopes (S) range from 0.75 to 0.98 and
332 coefficients (R^2) range from 0.80 to 0.98, respectively, between MOPITT, TES/MLS data
333 and the *Base* scenario output with the agreement generally highest during boreal winter and
334 lowest during boreal summer. However, the largest biases (Fig. 12) **Error! Reference**
335 **source not found.**occur over 1) tropical and subtropical biomass burning regions (~20%)
336 during boreal winter, indicating that either the CO emissions used in the *Base* scenario are
337 too high or that simulated OH is too low, and 2) most of the northern hemisphere (< -20%)
338 during the summer season, indicating that either CO emissions are too low or that OH levels

339 are too high, which is consistent with previous studies using similar emissions (e.g., Shindell
340 et al., 2006; Strode et al., 2015). In addition to possible biases associated with emissions,
341 some of the model-observation discrepancies may be associated with uncertainties in the
342 satellite datasets (Ho et al., 2009; Deeter et al., 2012; Amnuaylojaroen et al., 2014). Based
343 on direct comparison with Tall Tower measurements, Deeter et al. (2012) find that a
344 smoothing error, which depends on the retrieval averaging kernels and CO variability in the
345 lower troposphere, exhibits strong geographical and seasonal variability. Amnuaylojaroen et
346 al. (2014) find that simulated CO concentrations are significantly and consistently higher
347 than that of MOPITT V6 data over areas of biomass burning in Southeast Asia, similar to our
348 results.
349   The primary advantage of the TES/MLS joint CO product is that it gives information on
350 vertical distributions (Fig. 13). The simulation captures the tropospheric vertical profiles
351 reasonably well (within $\pm 1\sigma$ of TES/MLS mean) at the selected locations in the northern and
352 southern hemispheres and in all seasons, except over West Africa in boreal winter during the
353 peak of biomass burning. The adjustment of the simulated CO with the TES/MLS averaging
354 kernel (AK) significantly improves the agreement above 300 mb, over all locations and in all
355 seasons while near the surface the effect is geographically varying, in agreement with other
356 studies (e.g., Deeter et al., 2012). Over the eastern US, the adjustment of simulated CO
357 causes a slightly larger positive bias compared to that without adjustment. Though simulated
358 CO is significantly improved near the surface, it is still biased high over West Africa by
359 ~50% during the peak of biomass burning, also consistent with other studies
360 (Amnuaylojaroen et al., 2014).

4 ECCOH as a Tool for Studying the Nonlinear CH_4-CO-OH System

362   In this section, we 1) present the justification for simulating the nonlinear chemistry of the
363 CH_4-CO-OH system as opposed to using a static climatology of OH distributions, and 2)
364 demonstrate the utility of the ECCOH chemistry module for studying the CH_4-CO-OH
365 system. In Sect. 4.1, we discuss the nontrivial, large-scale interannual variations of methane,
366 CO, and OH in our scenarios. In Sect. 4.2, we discuss the considerable spatial and temporal
367 heterogeneity of OH and methane and CO loss rates, which would not be captured if a static
368 climatology of OH distributions was used. In Sect. 4.3, we present the results of our
369 sensitivity scenarios (Table 2), which demonstrate the utility of the ECCOH chemistry
370 module for studying the CH_4-CO-OH system.

4.1 Large Scale Interannual Variations in Methane, CO, and OH

372   Even on a global scale, there are large interannual variations in methane, CO, and OH.
373 The deviations of mass-weighted concentrations of methane, CO, and OH for both the *Base*
374 and *AllVary* scenarios are shown in Fig. 14. The magnitudes of the year-to-year deviations in
375 methane are not substantially different between the two scenarios, since the *Base* scenario
376 includes the important source of variation associated with anthropogenic methane emissions
377 and methane's background is large. On the other hand, the deviations for CO and OH are far
378 greater in the *AllVary* scenario. The magnitude of the CO deviations is a factor of ten greater
379 in the *AllVary* scenario than the *Base* scenario, which has annually-repeating CO emissions.

380   The magnitude of the OH deviations increase ±2% to ±5%, though as discussed below, there
381   are much larger variations on regional scales that are masked in the global average. In
382   general, CO and OH deviations are coincident, but of opposite sign as reaction of CO with
383   OH is the primary sink for both gases on a global scale. Similar deviations are seen in the
384   mid-latitudes of both hemispheres, indicating the global extent of some specific events, such
385   as large biomass burning events. These results are also consistent with Voulgarakis et al.
386   (2015) who, using full chemistry simulations, found large deviations (> 15%) in CO using
387   annually-varying CO biomass burning emissions as compared to annually-repeating
388   emissions.

389   The nonlinear effects of the CH$_4$-CO-OH system on the temporal evolution of global
390   mass-weighted methane are smaller, but significant, as compared to the effects of variations
391   of methane emissions. The $E_{CH4}Vary$ scenario includes variations in anthropogenic and
392   natural methane emissions and also variations in meteorology (e.g., temperature, water
393   vapor) that influence the distributions of methane, CO, and OH. The *AllVary* scenario
394   includes also variations in CO emissions and all the other factors that influence OH, such as
395   the overhead ozone column, NO$_x$, tropospheric ozone, and VOCs. The influence of the
396   nonlinear effects of the CH$_4$-CO-OH system is shown in the difference of the *AllVary* and
397    $E_{CH4}Vary$ scenarios. For example, the shaded area between the two scenarios in Fig. 4
398   illustrates the combined effect of nonlinearities of the CH$_4$-CO-OH system on methane's
399   growth rate. The growth rate in the *AllVary* scenario is about 4 ppb/yr higher than in the
400    $E_{CH4}Vary$ scenario during the early 1990s, a time when stratospheric ozone was impacted by
401   the eruption of Mt. Pinatubo, emissions from the Soviet Union changed as it contracted
402   economically, and there was a prolonged El Niño. While these factors caused changes in
403   methane emissions, they also caused substantial variations in CO and OH (Duncan and
404   Logan, 2008) that influenced methane's growth rate. Briefly in the mid-1990s, the growth
405   rate in the *AllVary* scenario becomes lower than in the $E_{CH4}Vary$ scenario. The decline in
406   methane growth rate in 1994-1997 is primarily related to the variability of the factors that
407   influence OH (Fig. S 4) while the other non-linear feedbacks are primarily related to
408   variability in CO emissions (Fig. S 5). Worldwide, there were record wildfires in 1997 and
409   1998 that were associated with a record El Niño, which began in 1997, that transitioned to a
410   record La Niña in 1998 (Duncan et al., 2003a, 2003b). Consequently, there were large
411   variations in CO (Duncan and Logan, 2008) that causes methane's growth rate to become
412   higher again in the *AllVary* scenario. During the 2000s, a relatively quiet period with few
413   large wildfires or notable ENSO events, the growth rate is lower in the *AllVary* than the
414    $E_{CH4}Vary$ scenario. In summary, the nonlinear effects of the CH$_4$-CO-OH system cause
415   important fluctuations in methane's growth rate over our study period of ±4 ppb/yr.

416   We compare simulated, mass-weighted pseudo first order rate constants (k'), a proxy for
417   OH interannual variations, from each of our scenarios to that inferred from MCF
418   measurements (Fig. 15; 1998-2007; Montzka et al., 2011). We find that none of our model
419   scenarios are able to reproduce the inferred interannual OH variability of Montzka et al.
420   (2011), though the simulated variability is of similar magnitude and within observational
421   uncertainty. Our findings are consistent with other modeling studies (Montzka et al., 2011;
422   Holmes et al., 2013; Murray et al., 2013 and references therein). While global interannual
423   variations are informative, there can be considerable OH interannual variations regionally (as

424　discussed in Sections 4.2 and 4.3) that may not be reflected in the global average (Lelieveld
425　et al., 2002; Wild and Palmer, 2008).

426　Despite the lack of agreement between the inferred and simulated OH variations, this
427　comparison exercise allows us to understand the contribution of various factors to the
428　simulated interannual variations of tropospheric OH and, subsequently, the growth rate of
429　methane (Fig. 4). As shown in Fig. 15, the *Base* scenario has ±3% interannual variability.
430　This scenario includes interannual variations in meteorology, such as in clouds, water vapor,
431　temperature and solar radiation, which are known to be important drivers of OH (e.g., Rohrer
432　and Berresheim, 2006; Rohrer et al., 2014). The only large deviation in OH from the *Base*
433　scenario occurs in 1997 and 1998 in the $BBE_{CO}Vary$ scenario. There were several major
434　wildfires that account for this deviation, including fires in Indonesia, Mexico, and the boreal
435　forests of Asia and North America (e.g., Duncan et al., 2003a). OH is lower in the *AllVary*
436　scenario than the *Base* scenario because of higher CO emissions from the fires. For instance,
437　Duncan et al. (2003b) used a model to show that the Indonesian wildfires in 1997 depressed
438　OH levels by more than 20% over the Indian Ocean and 5-10% over much of the tropics for
439　several months. Lower OH during 1997 and 1998 in the *AllVary* scenario is consistent with
440　the higher methane growth rate as compared to the *Base* scenario (Fig. 3).

441　ENSO affects the variability of sea surface temperatures, water vapor, deep convection,
442　etc., and, subsequently, OH over large regions of the tropics. As shown in Fig. 16, the
443　deviations of mass-weighted OH from various scenarios over Indonesia (100°-150°E; 6°N-
444　6°S) are generally anti-correlated with the Multivariate ENSO Index (MEI, Wolter et al.,
445　2011), a proxy of ENSO. OH variations in the *Base* scenario, which includes meteorological
446　variations that affect OH via variations in water vapor, clouds, etc., are ±4% ($R^2 = 0.20$), but
447　much higher in the scenarios that include variations in biomass burning emissions (e.g.,
448　*AllVary* scenario), which better capture the ENSO variability ($R^2 = 0.59$).

4.2　Spatial and Temporal Distributions of the Production/Loss Rates of Methane and CO

451　Any model simulation using annually-repeating and archived OH will not accurately
452　capture regional and interannual variations in the loss rates of methane and CO. A
453　simulation using zonally-averaged archived OH (e.g., Spivakovsky et al., 2000), such as was
454　done in the TransCom MIP, will not capture any regional and interannual variations. For
455　example, Fig. S 7 and Fig. S 12 reproduce Fig. 4a and Fig. 5, respectively, but include
456　methane from a simulation using archived and annually-repeating OH of the NASA Global
457　Modeling Initiative (GMI) model (Duncan et al., 2007b; Strahan et al., 2007). The simulated
458　longer methane lifetime (Fig. S 7), using archived OH, leads to an accumulation of methane
459　over the multi-decadal simulation. In this situation, the archived OH would need to be
460　adjusted higher to improve the simulation of methane as compared to observations.

461　Even though methane is relatively well mixed in the troposphere due to its long lifetime,
462　there is important spatial heterogeneity in methane's and CO's loss rates (Fig. 17 to Fig.
463　21), which is associated with the distribution of sources and reaction with OH, and changes
464　in the density of air with altitude. The global methane loss rate maximizes during boreal
465　summer and reaches a minimum during boreal winter (Fig. 17). Most methane loss occurs

466 between 30ºS and 30ºN (Fig. 17) since OH is most abundant in this region and methane's
467 reaction with OH is temperature dependent (Sander et al., 2011). In addition, most loss
468 occurs near the surface despite higher OH in the mid-troposphere (Fig. 2) because of higher
469 methane mole fractions near the surface (e.g., ~3 % over Alaska, but higher over source
470 regions), the altitude dependence of air density, and the temperature dependence of the loss
471 rate (Fig. 18). Methane's loss rates in the *AllVary* scenario are relatively higher, especially
472 over biomass burning regions (Fig. 17) and have much higher spatial variability than in the
473 *Base* scenario (Fig. 19). In contrast to methane, a higher proportion of CO is lost at
474 northern hemisphere mid-latitudes as the CO loss rate is less temperature dependent than
475 methane's and the lifetime is shorter (Fig. 20). The CO loss rate also varies strongly with
476 altitude (not shown), similar to that of methane. The simulated seasonal mean loss rate of
477 CO from the *AllVary* scenario is also relatively higher over biomass burning regions but
478 lower over Asia (Fig. 20), and has much higher variability that reaches up to ~20%
479 compared to about 5% in the *Base* scenario (Fig. 21).

4.3   Factors that Influence the Nonlinear CH_4-CO-OH System

481   The differences in global abundances of CO and OH between our least complex (*Base,*
482 Table 1) and most complex (*AllVary*, Table 2) scenarios are substantial and their impact on
483 methane's evolution is nontrivial as discussed in Sect. 4.1 and 4.2. Therefore, model studies
484 of methane and/or CO, which use archived fields of OH distributions, will not capture these
485 important nonlinear feedbacks of the CH_4-CO-OH system (e.g., Fig. 4). Here, we discuss the
486 contribution of various factors to the observed spatial distributions and temporal evolution of
487 observed methane, CO, and OH to demonstrate the utility of the ECCOH chemistry module
488 for studying the CH_4-CO-OH system. We provide a brief summary of our conclusions from
489 the scenarios at the end of this section.
490 $E_{CH4}Vary$ *Scenario*: In the $E_{CH4}Vary$ scenario, all methane emissions are annually-varying
491 (Fig. S 1). Variations in emissions from wetlands are the largest single contributor to global
492 interannual variations, with biomass burning being a lesser contributor (e.g., Bousquet et al.,
493 2006). Patra et al. (2011) reported that up to 60% of methane's observed interannual
494 variation can be explained by variations in meteorology as well as interannual variations in
495 wetland and biomass burning emissions. Given the high methane background concentration,
496 the spatial differences of methane columns between the $E_{CH4}Vary$ and *Base* scenarios are
497 rather small (about ±5 ppb (-1 to 1%)) over most of the globe when taken as seasonal
498 averages of 1988-2007 (Fig. S 19). Consistent with the annually-varying natural emissions
499 of methane, the largest differences occur over rice-producing regions of India and
500 Bangladesh (up to ~5%)) and the wetlands of South America (down to -5%), including the
501 Pantanal. The simulated methane monthly variations from the $E_{CH4}Vary$ scenario are in better
502 agreement for the northern hemisphere high latitude GMD station observations as compared
503 to the *Base* scenario (Fig. S 8), which is also consistent with the findings of the TransCom
504 MIP (Patra et al., 2011). The impact of annually-varying natural methane emissions has a
505 small effect (-1% to 1%), as expected, on the spatial distributions of CO and OH because of
506 the slow reaction rate of methane with OH (Fig. S 19; Table 4).

507 *BBE$_{CO}$Vary* and *FFBBE$_{CO}$Vary Scenarios*: We developed these scenarios to understand the
508 influence of annually-varying CO emissions from biomass burning and fossil fuel
509 combustion (Fig. S 2) on the observed interannual variation of methane, CO and OH.
510 Including annually-varying biomass burning emissions (*BBE$_{CO}$Vary*) improves the mean
511 agreement of the simulated CO with GMD observations (mean S=0.83, R^2 = 0.70, Table 4),
512 but not at all individual GMD stations (Table 4). Improvements occur particularly during
513 years with large fires (e.g., 1997, 1998, 2003, 2004; Fig. 9 to Fig. 11). Adding annually-
514 varying anthropogenic CO emissions in addition to annually-varying biomass burning
515 emissions (*FFBBE$_{CO}$Vary*) further improves the mean comparison (mean S=0.88),
516 particularly in the northern hemisphere during the 1990s (Fig. 10). Overall, annually-varying
517 CO emissions (*FFBBE$_{CO}$Vary*) have a significant impact on the spatial distributions of
518 tropospheric CO (±20%) and OH (±10%) relative to the *Base* scenario, and influence
519 methane by ±1% (Fig. S 21, Table 4). Simulating annually-varying CO biomass burning
520 emissions (i.e., *BBE$_{CO}$Vary* scenario) improves simulated methane relative to the *Base*
521 scenario as compared to observations (mean S=0.97, R^2= 0.76, Table 4).
522 *OH$_{input}$Vary* Scenario: In this scenario, we look at the impact of other causal factors that
523 influence OH, including trends in NO$_x$ and VOC emissions and the overhead ozone column
524 (Table 2). For example, both variations in the overhead ozone column and NO emissions
525 from lightning are known to cause variations in global OH (e.g., Duncan and Logan, 2008;
526 Murray et al., 2013). Together, these causal factors have a significant influence on the spatial
527 distributions of OH (±20%) and CO (±5%) relative to the *Base* scenario and a ±1% effect on
528 methane (Fig. S 4, Fig. S 20, Table 4).
529 *AllVary Scenario*: In this scenario, we investigate the combined effect of all variables (Table
530 2) on the simulated distributions of methane, CO, and OH. The seasonal mean spatial (not
531 shown) and zonal (Fig. 2) distributions of OH are quite comparable to that of the *Base*
532 scenario. The interannual variations in the seasonal mean OH (Fig. 22) are significantly
533 higher (~20%) as compared to the *Base* scenario (<5%, sec. 3.1), which is related to the
534 annually-varying methane and CO emissions as well as OH constraints in this scenario.
535 There are large differences in the spatial distributions of methane (±5%), CO (±20%), and
536 OH (±20%) between the *Base* and *AllVary* scenarios (Fig. S 22, Table 4). Despite large
537 spatial differences in OH, the global, mean MCF lifetime for the *AllVary* scenario, which
538 ranges from 6.01 (±0.51) to 6.67 (±0.61) years over the simulation period, is not significantly
539 different from that of the *Base* scenario.
540   *Summary of Key Findings of Sensitivity Studies:* Overall, variations in anthropogenic and
541 natural methane emissions drive the majority of global variations in observed methane and
542 variations in anthropogenic and natural CO emissions drive the majority of global variations
543 in observed CO. These results are consistent with the findings of other literature studies
544 (e.g., Duncan and Logan, 2008; Patra et al., 2011). We find that the influence of variations of
545 CO emissions and factors that influence OH (e.g., overhead ozone column, VOCs, NO$_x$)
546 have a significant net effect on the distributions and temporal evolution of methane, CO and
547 OH. This result is consistent with the findings of Duncan and Logan (2008) for CO and OH.
548 The significant influence of the combined nonlinear feedbacks on methane is shown in the
549 difference of the *AllVary* and *E$_{CH4}$Vary* scenarios (e.g., Fig. 4).
550   Accurate quantification of the magnitude of the combined nonlinear feedbacks is

551 ultimately dependent on the uncertainties and errors of emissions, such as those discussed in
552 Sect. 3, and independent variables, each of which have their own uncertainties, used in the
553 parameterization of OH. With our sensitivity simulations, we discussed instances when
554 changes to emissions and/or the input to the parameterization of OH improved or worsened
555 the simulated methane and CO. In some instances, simulated methane and/or CO from the
556 least complex *Base* scenario more favorably agreed with observations than the other more
557 complex scenarios, including methane in the most complex *AllVary* scenario (e.g., Table 4,
558 Fig. 4). However, in these instances, better correlation does not necessarily imply that a
559 simpler scenario, such as the *Base* scenario or a scenario that uses archived and annually-
560 repeating OH, is inherently better. The best scenario is one that accurately simulates the
561 complex interactions of the factors that influence the CH_4-CO-OH system, which will give
562 confidence in the response of the system to perturbations, such as from large interannual
563 variations in wetland fluxes, biomass burning, ENSO, and volcanic eruptions. The next steps
564 for our research include quantifying the 1) sensitivity of the simulated CH_4-CO-OH system
565 to uncertainties in the factors (e.g., water vapor, clouds, trace gases) that control tropospheric
566 OH so as to improve simulated methane and CO with observations, and 2) the influence of
567 potential large atmospheric carbon perturbations in a warming world, such as may occur
568 from permafrost thaw, methane hydrate release, and enhanced biomass burning.

569 5   Summary

570   We present the fully interactive, computationally <u>E</u>fficient <u>CH4</u>-<u>C</u>O-<u>OH</u> (ECCOH)
571 chemistry module, which we implemented in the NASA GEOS-5 AGCM. To demonstrate
572 the utility of the ECCOH chemistry module, we exercised the module with a set of scenarios
573 to simulate the influence of various causal factors on OH and the observed variations in
574 methane and CO over 1988-2007, which gives confidence in the fidelity of the module for
575 scientific research. Discrepancies between the output and observations are largely explained
576 by known deficiencies (as reported in the literature) in the methane and CO emissions used
577 as input to the ECCOH chemistry module and AGCM. Through our simulations, we show
578 the importance of using an interactive CH_4-CO-OH system as opposed to using static,
579 archived OH fields, as nonlinear feedbacks on methane, CO, and OH are non-trivial. For
580 example, nonlinear feedbacks modulate the global methane growth rate over our study
581 period (± 20 ppbv yr^{-1}) by ± 4 ppbv yr^{-1} (Fig. 4)."
582
583

Code availability
585 The GEOS-5 source code is available under the NASA Open-Source Agreement at
586 http://opensource.gsfc.nasa.gov/projects/GEOS-5/.
587 The GEOS-5 CCM version that includes our ECCOH chemistry module is available
588 in the supplementary material. For documentation and installation instructions, please visit
589 the   GEOS-5   online   wiki: http://geos5.org/wiki/index.php?title=GEOS-
590 5_Earth_System_Modeling_and_Data_Assimilation.
591

6   References

Amnuaylojaroen, T., Barth, M. C., Emmons, L. K., Carmichael, G. R., Kreasuwun, J., Prasitwattanaseree, S., and Chantara, S.: Effect of different emission inventories on modeled ozone and carbon monoxide in Southeast Asia, Atmos. Chem. Phys., 14, 12983-13012, doi:10.5194/acp-14-12983-2014, 2014.

Bousquet, P., Ciais, P., Miller, J. B., Dlugokencky, E. J., Hauglus- taine, D. A., Prigent, C., Van der Werf, G. R., Peylin, P., Brunke, E. G., Carouge, C., Langenfelds, R. L., Lathiere, J., Papa, F., Ra- monet, M., Schmidt, M., Steele, L. P., Tyler, S. C., and White, J.: Contribution of anthropogenic and natural sources to atmospheric methane variability, Nature, 443, 439–443, 2006.

Chameides, W., Liu, S. C. and Cicerone, R. J.: Possible variations in atmospheric methane, J. Geophys. Res., 81, 4997-5001, 1976.

Deeter, M. N.: MOPITT (Measurement of Pollution in the Troposphere) Version6 Product User'sGuide, available at: http://www2.acd.ucar.edu/sites/default/files/mopitt/v6_users_guide_201309.pdf (last access: May 28th 2015), 2013.

Deeter, M. N., Worden, H. M., Edwards, D. P., Gille, J. C., and Andrews, A. E.: Evaluation of MOPITT retrievals of lower tropospheric carbon monoxide over the United States, J. Geophys. Res., 117, D13306, doi:10.1029/2012JD017553, 2012.

Dlugokencky, E.J., Lang, P.M., and Masarie, K.A., Atmospheric Methane Dry Air Mole Fractions from the NOAA ESRL Carbon Cycle Cooperative Global Air Sampling Network, 1983-2009, Version: 2010-08-12, Path: ftp://ftp.cmdl.noaa.gov/ccg/ch4/flask/-event/, 2010.

Dlugokencky, E.J., Lang, P.M., Crotwell, A.M., Masarie, K.A., and Crotwell, M.J.: Atmospheric Methane Dry Air Mole Fractions from the NOAA ESRL Carbon Cycle. Cooperative Global Air Sampling Network, 1983-2013, Version: 2014-06-24, 2014.

Duncan, B. N., Portman, D., Bey, I., and Spivakovsky, C. M.: Parameterization of OH for efficient computation in chemical tracer models, J. Geophys. Res., 105 (D10), 12259–12262, 2000.

633 Duncan, B. N., Martin, R. V., Staudt, A. C., Yevich, R. M., and Logan, J. A.: Interannual and
634   Seasonal Variability of Biomass Burning Emissions Constrained by Satellite Observations,
635   J. Geophys. Res., 108(D2), 4040, doi:10.1029/2002JD002378, 2003a.

636 Duncan, B.N., I. Bey, M. Chin, L.J. Mickley, T.D. Fairlie, R.V. Martin, and H. Matsueda,
637   Indonesian Wildfires of 1997: Impact on Tropospheric Chemistry, J. Geophys. Res., 108,
638   D15, 4458, doi:10.1029/2002JD003195, 2003b.

639 Duncan, B. N., Logan, J. A., Bey, I., Megretskaia, I. A., Yantosca, R. M., Novelli, P. C.,
640   Jones, N. B., and Rinsland, C. P.: Global budget of CO, 1988–1997: Source estimates and
641   validation with a global model, J. Geophys. Res., 112(D22), D22301,
642   doi:10.1029/2007JD008459, 2007a.

643 Duncan, B. N., Strahan, S. E., Yoshida, Y., Steenrod, S. D., and Livesey, N.: Model study of
644   the cross-tropopause transport of biomass burning pollution, Atmos. Chem. Phys., 7,
645   3713–3736, doi:10.5194/acp-7-3713-2007, 2007b.

646 Duncan, B. and Logan, J.: Model analysis of the factors regulating the trends and variability
647   of carbon monoxide between 1988 and 1997, Atmos. Chem. Phys., 8, 7389-7403, 2008.

648 Elshorbany, Y. F, Barnes, I., Becker, K. H, Kleffmann, J., and Wiesen, P.: Sources and
649   Cycling of Tropospheric Hydroxyl Radicals-An Overview, Zeitschrift für Physikalische
650   Chemie, 224, 967-987, DOI:10.1524/zpch.2010.6136, 2010.

651 Elshorbany, Y. F., Kleffmann, J., Hofzumahaus, A., Kurtenbach, R., Wiesen, P., Dorn,H.-P.,
652   Schlosser, E., Brauers, T., Fuchs, H., Rohrer, F., Wahner, A., Kanaya, Y., Yoshino, A.,
653   Nishida, S., Kajii, Y., Martinez, M., Rudolf, M., Harder, H., Lelieveld, J., Elste, T., Plass-
654   Dülmer, C., Stange, G., and Berresheim, H.: HOx Budgets during HOxComp: a Case
655   Study of HO_x Chemistry under NO_x limited Conditions, J. Geoophys. Res., 117, D03307,
656   doi: 10.1029/2011JD017008, 2012a.

657 Elshorbany, Y. F., Steil, B., Brühl, C., and Lelieveld, J.: Impact of HONO on global
658   atmospheric chemistry calculated with an empirical parameterization in the EMAC model,
659   Atmos. Chem. Phys., 12, 9977-10000, doi:10.5194/acp-12-9977-2012, 2012b.

660 Elshorbany, Y. F., Crutzen, P. J., Steil, B., Pozzer, A., Tost, H., and Lelieveld, J.: Global and
661   regional impacts of HONO on the chemical composition of clouds and aerosols, Atmos.
662   Chem. Phys., 14, 1167-1184, doi:10.5194/acp-14-1167-2014, 2014.

663 Fiore, A. M., Jacob, D. J., Field, B. D., Streets, D. G., Fernandes, S. D., and Jang, C. :
664   Linking air pollution and climate change: The case for controlling methane, Geophys. Res.
665   Lett., 29(19), 1919, doi:10.1029/2002GL015601, 2002.

666 Fiore, A. M., Horowitz, L. W., Dlugokencky, E. J. and West, J. J.: Impact of meteorology
667   and emissions on methane trends, 1990-2004, Geophys. Res. Lett., 33, L12809,
668   doi:10.1029/2006GL026199, 2006.

669 Fiore, A.M., Dentener, F.J., Wild, O., Cuvelier, C., Schultz, M.G., Hess, P., Textor, C.,
670   Schulz, M., Doherty, R.M., Horowitz, L.W., MacKenzie, I.A., Sanderson, M.G., Shindell,
671   D.T., Stevenson, D.S., Szopa, S., Van Dingenen, R., Zeng, G., Atherton, C., Bergmann,
672   D., Bey, I., Carmichael, G., Collins, W.J., Duncan, B.N., Faluvegi, G., Folberth, G.,
673   Gauss, M., Gong, S., Hauglustaine, D., Holloway, T., Isaksen, I.S.A., Jacob, D.J., Jonson,
674   J.E., Kaminski, J.W., Keating, T.J., Lupu, A., Marmer, E., Montanaro, V., Park, R.J.,
675   Pitari, G., Pringle, K.J., Pyle, J.A., Schroeder, S., Vivanco, M.G., Wind, P., Wojcik, G.,

676   Wu, S., Zuber, A.: Multimodel estimates of intercontinental source-receptor relationships
677   for ozone pollution, J. Geophys. Res., 114, D04301, doi:10.1029/2008JD010816, 2009.

678   Fujino J, Nair R, Kainuma M, Masui T, Matsuoka Y, Multigas mitigation analysis on
679   stabilization scenarios using aim global model. The Energy Journal Special issue #3:343–
680   354, 2006.

681   Frankenberg, C., Aben, I., Bergamaschi, P., Dlugokencky, E. J., van Hees, R., Houweling,
682   S., van der Meer, P., Snel, R., Tol, P.: Global column-averaged methane mixing ratios from
683   2003 to 2009 as derived from SCIAMACHY: Trends and variability, J. of Geophys. Res.,
684   116, D04302, doi: 10.1029/2010JD014849, 2011.

685   Fuchs, H., Hofzumahaus, A., Rohrer, F., Bohn, B., Brauers, T., Dorn, H.-P., Ha€seler, R.,
686   Holland, F., Kaminski, M., Li, X., Lu, K., Nehr, S., Tillmann, R., Wegener, R., Wahner,
687   A.: Experimental evidence for efficient hydroxyl radical regeneration in isoprene
688   oxidation. Nat. Geosci. 6, 1023-1026, doi:10.1038/ngeo1964, 2013.

689   Giglio, L., Randerson, J. T., van der Werf, G. R., Kasibhatla, P. S., Collatz, G. J., Morton, D.
690   C., and DeFries, R. S.: Assess- ing variability and long-term trends in burned area by
691   merging multiple satellite fire products, Biogeosciences, 7, 1171–1186, doi:10.5194/bg-7-
692   1171-2010, 2010.

693   Gloudemans, A. M. S., Schrijver, H., Hasekamp, O. P., and Aben, I.: Error analysis for CO
694   and CH4 total column retrievals from SCIAMACHY 2.3 μm spectra, Atmos. Chem. Phys.,
695   8, 3999-4017, doi:10.5194/acp-8-3999-2008, 2008.

696   Hijioka Y, Matsuoka Y, Nishimoto H, Masui T, Kainuma M.: Global GHG emission
697   scenarios under GHG concentration stabilization targets. J Glob Environ Eng 13:97–108,
698   2008.

699   Ho, S.-P., Edwards, D. P., Gille, J. C., Luo, M., Osterman, G. B., Kulawik, S. S., and
700   Worden, H.: A global comparison of carbon monoxide profiles and column amounts from
701   Tropospheric Emission Spectrometer (TES) and Measurements of Pollution in the
702   Troposphere (MOPITT), J. Geophys. Res., 114, D21307, doi:10.1029/2009JD012242,
703   2009.

704   Holmes, C. D., Prather, M. J., Søvde, O. A., and Myhre, G.: Future methane, hydroxyl, and
705   their uncertainties: key climate and emission parameters for future predictions, Atmos.
706   Chem. Phys., 13, 285-302, doi:10.5194/acp-13-285-2013, 2013.

707   Houweling, S., Krol, M., Bergamaschi, P., Frankenberg, C., Dlugokencky, E. J., Morino, I.,
708   Notholt, J., Sherlock, V., Wunch, D., Beck, V., Gerbig, C., Chen, H., Kort, E. A.,
709   Röckmann, T., and Aben, I.: A multi-year methane inversion using SCIAMACHY,
710   accounting for systematic errors using TCCON measurements, Atmos. Chem. Phys., 14,
711   3991-4012, doi:10.5194/acp-14-3991-2014, 2014.

712   Lamarque, J.-F., Shindell, D. T., Josse, B., Young, P. J., Cionni, I., Eyring, V., Bergmann,
713   D., Cameron-Smith, P., Collins, W. J., Doherty, R., Dalsoren, S., Faluvegi, G., Folberth,
714   G., Ghan, S. J., Horowitz, L. W., Lee, Y. H., MacKenzie, I. A., Nagashima, T., Naik, V.,
715   Plummer, D., Righi, M., Rumbold, S. T., Schulz, M., Skeie, R. B., Stevenson, D. S.,
716   Strode, S., Sudo, K., Szopa, S., Voulgarakis, A., and Zeng, G.: The Atmospheric
717   Chemistry and Climate Model Intercomparison Project (ACCMIP): overview and
718   description of models, simulations and climate diagnostics, Geosci. Model Dev., 6, 179–
719   206, doi:10.5194/gmd-6-179-2013, 2013.

720 Lawrence, M. G., Jöckel, P., and von Kuhlmann, R.: What does the global mean OH
721   concentration tell us?, Atmos. Chem. Phys., 1, 37-49, doi:10.5194/acp-1-37-2001, 2001.
722 Lelieveld, J., Peters, W., Dentener, F. J., and Krol, M. C.: Stability of tropospheric hydroxyl
723   chemistry, J. Geophys. Res., 107(D23), 4715, doi:10.1029/2002JD002272, 2002.
724 Lin, S.-J.: A "vertically Lagrangian" finite-volume dynamical core for global models, Mon.
725   Weather Rev., 132(10), 2293–2307, 2004.
726 Luo, M., Read, W., Kulawik, S., Worden, J., Livesey, N., Bowman, K. and Herman, R.:
727   Carbon monoxide (CO) vertical profiles derived from joined TES and MLS measurements,
728   J. Geophys. Res. Atmos., 118, 10601–10613, doi:10.1002/jgrd.50800, 2013.
729 Molod, A., Takacs, L., Suarez, M., Bacmeister, J., Song, I.-S., and Eichmann, A.: The
730   GEOS-5 Atmospheric General Circulation Model: Mean Climate and Development from
731   MERRA to Fortuna, NASA/TM–2012-104606, Technical Report Series on Global
732   Modeling and Data Assimilation, Vol. 28, edited by: Suarez, M., available at:
733   http://gmao.gsfc.nasa.gov/pubs/docs/tm28.pdf (last access: October 27, 2015), 2012.
734 Monks, S. A., Arnold, S. R., Emmons, L. K., Law, K. S., Turquety, S., Duncan, B. N.,
735   Flemming, J., Huijnen, V., Tilmes, S., Langner, J., Mao, J., Long, Y., Thomas, J. L.,
736   Steenrod, S. D., Raut, J. C., Wilson, C., Chipperfield, M. P., Diskin, G. S.,
737   Weinheimer, A., Schlager, H., and Ancellet, G.: Multi-model study of chemical and
738   physical controls on transport of anthropogenic and biomass burning pollution to the
739   Arctic, Atmos. Chem. Phys., 15, 3575-3603, doi:10.5194/acp-15-3575-2015, 2015.
740 Montzka, S. A., Krol, M., Dlugokencky, E., Hall, B., Joeckel, P., and Lelieveld, J.: Small
741   interannual variability of global atmospheric hydroxyl, Science, 331, 67-69,
742   doi:10.1126/science.1197640, 2011.
743 Murray, L. T., Logan, J. A., and Jacob, D., J.:, Interannual variability in tropical tropospheric
744   ozone and OH: The role of lightning, J. Geophys. Res. Atmos., 118, 11,468–11,480,
745   doi:10.1002/jgrd.50857, 2013.
746 Myhre, G., Shindell, D., Breìon, F.-M., Collins, W., Fuglestvedt, J., Huang, J., Koch, D.,
747   Lamarque, J.-F., Lee, D., 5 Mendoza, B., Nakajima, T., Robock, A., Stephens, G.,
748   Takemura, T., and Zhang, H.: Anthropogenic and natural radiative forcing, in: Climate
749   Change 2013: The Physical Science Basis. Contribution of Working Group I to the Fifth
750   Assessment Report of the Intergovernmental Panel on Climate Change, edited by: Stocker,
751   T. F., Qin, D., Plattner, G.-K., Tignor, M., Allen, S. K., Boschung, J., Nauels, A., Xia, Y.,
752   Bex, V., and Midgley, P. M., availa1able at:
753   http://www.climatechange2013.org/images/report/WG1AR5_ALL_FINAL.pdf (last
754   access: October 27, 2015), 2013.
755 Naik, V., Voulgarakis, A., Fiore, A. M., Horowitz, L. W., Lamarque, J.-F., Lin, M.,
756   Prather, M. J., Young, P. J., Bergmann, D., Cameron-Smith, P. J., Cionni, I.,
757   Collins, W. J., Dalsøren, S. B., Doherty, R., Eyring, V., Faluvegi, G., Folberth, G. A.,
758   Josse, B., Lee, Y. H., MacKenzie, I. A., Nagashima, T., van Noije, T. P. C.,
759   Plummer, D. A., Righi, M., Rumbold, S. T., Skeie, R., Shindell, D. T., Stevenson, D. S.,
760   Strode, S., Sudo, K., Szopa, S., and Zeng, G.: Preindustrial to present-day changes in
761   tropospheric hydroxyl radical and methane lifetime from the Atmospheric Chemistry and
762   Climate Model Intercomparison Project (ACCMIP), Atmos. Chem. Phys., 13, 5277-5298,
763   doi:10.5194/acp-13-5277-2013, 2013.

764 Novelli, P., Steele, P., Tans, P. P.: Mixing ratios of carbon monoxide in the troposphere, J.
765   Geophys. Res., 102, 12,855-12,861, doi: 10.1029/92JD02010, 1992.

766 Novelli, P., Masarie, K., A., Lang, P. M.: Distributions and recent changes in carbon
767   monoxide in the lower troposphere, J. Geosphys. Res., 103, 19,015-19,033, 1998.

768 Oman, L. D., J. R. Ziemke, A. R. Douglass, D. W. Waugh, C. Lang, J. M. Rodriguez, and J.
769   E. Nielsen (2011), The response of tropical tropospheric ozone to ENSO, Geophys. Res.
770   Lett., 38, L13706, doi:10.1029/2011GL047865, 2011.

771 Ott, L., Duncan, B., Pawson, S., Colarco, P., Chin, M., Randles, C., Diehl, T., and Nielsen,
772   E.: Influence of the 2006 Indonesian biomass burning aerosols on tropical dynamics
773   studied with the GEOS5 AGCM, J. Geophys. Res., 115, D14121,
774   doi:10.1029/2009JD013181, 2010.

775 Patra, P. K., Houweling, S., Krol, M., Bousquet, P., Belikov, D., Bergmann, D., Bian, H.,
776   Cameron-Smith, P., Chipperfield, M. P., Corbin, K., Fortems-Cheiney, A., Fraser, A.,
777   Gloor, E., Hess, P., Ito, A., Kawa, S. R., Law, R. M., Loh, Z., Maksyutov, S., Meng, L.,
778   Palmer, P. I., Prinn, R. G., Rigby, M., Saito, R., and Wilson, C.: TransCom model
779   simulations of CH_4 and related species: linking transport, surface flux and chemical loss
780   with CH_4 variability in the troposphere and lower stratosphere, Atmos. Chem. Phys., 11,
781   12813-12837, doi:10.5194/acp-11-12813-2011, 2011.

782 Patra, P. K., Krol, M. C., Montzka, S. A., Arnold, T., Atlas, E. L., Lintner, B. R., Xiang B.,
783   Elkins J. W., Fraser P. J., Ghosh A., Hintsa E.J., Hurst D. F., Ishijima K., Krummel P. B.,
784   Miller B. R., Miyazaki K., Moore F. L, Mühle J., O'Doherty S., Prinn R. G., Steele L. P.,
785   Takigawa M., Wang H. J., Weiss R. F., Wofsy S. C., Young, D.: Observational evidence
786   for interhemispheric hydroxyl-radical parity. Nature, 513(7517), 219-23, doi:
787   10.1038/nature13721, 2014.

788 Pawson, S., R., Stolarski, S., Douglass, A. R. , Newman, P. A., Nielsen, J. E., Frith, S. M.,
789   and Gupta, M. L.: Goddard Earth Observing System chemistry-climate model simulations
790   of stratospheric ozone-temperature coupling between 1950 and 2005, J. Geophys. Res.,
791   113, D12103, doi:10.1029/2007JD009511, 2008.

792 Prather, M., and Spivakovsky, C. M.: Tropospheric OH and the lifetimes of
793   hydrochlorofluorocarbons, J. Geophys. Res., 95(D11), 18723–18729,
794   doi:10.1029/JD095iD11p18723, 1990.

795 Prather, M.: Lifetimes and Eigen states in atmospheric chemistry, Geophys. Res. Lett., 21, 9,
796   801-804, 1994.

797 Prather, M.: Time scales in atmospheric chemistry: Theory, GWPs for CH_4 and CO, and
798   runaway growth, Geophys. Res. Lett., 23, 19, 2597–2600, DOI: 10.1029/96GL02371,
799   1996.

800 Prather, M. J., C. D. Holmes, and J. Hsu.: Reactive greenhouse gas scenarios: Systematic
801   exploration of uncertainties and the role of atmospheric chemistry, Geophys. Res. Lett.,
802   39, L09803, doi:10.1029/2012GL051440, 2012.

803 Prinn, R. G., Huang, J., Weiss, R. F., Cunnold, D. M., Fraser, P. J., Simmonds, P. G.,
804   McCulloch, A., Harth, C., Reimann, S., Salameh, P., O'Doherty, S., Wang, R. H. J.,
805   Porter, L. W., Miller, B. R., and Krummel, P. B.: Evidence for variability of atmospheric
806   hydroxyl radicals over the past quarter century, Geophys. Res. Lett., 32, L07809,
807   doi:10.1029/2004GL022228, 2005.

808 Randerson, J.T., G.R. van der Werf, L. Giglio, G.J. Collatz, and P.S. Kasibhatla.. Global Fire
809　　Emissions Database, Version 3 (GFEDv3.1). Data set. Available at: http://daac.ornl.gov
810　　(last access: October 27, 2015) from Oak Ridge National Laboratory Distributed Active
811　　Archive Center, Oak Ridge, Tennessee, USA. doi:10.3334/ORNLDAAC/1191, 2013.

812 Rienecker, M. M., Suarez , M. J., Todling, R., Bacmeister, J., Takacs, L., Liu, H.-C., Gu, W.,
813　　Sienkiewicz, M., Koster, R. D., Gelaro, R., Stajner, I., and Nielsen, J. E.: The GEOS-5
814　　data assimilation system − Documentation of Versions 5.0.1, 5.1.0, and 5.2.0, Technical
815　　Report Series on Global Modeling and Data Assimilation, Vol. 27, available at:
816　　http://gmao.gsfc.nasa.gov/pubs/docs/GEOS5_104606-Vol27.pdf (last access: October 27,
817　　2015), 2008.

818 Rohrer, F., and Berresheim, H.: Strong correlations between levels of tropospheric hydroxyl
819　　radicals and solar ultraviolet radiation, Nature, 442, 184-187, doi:10.1038/nature04924,
820　　2006.

821 Rohrer, F., Lu, K., Hofzumahaus, A., Bohn, B., Brauers, T., Chang, C.-C., Fuchs, H.,
822　　Häseler, R., Holland, F., Hu, M., Kita, K., Kondo, Y., Li, X., Lou, S., Oebel, A., Shao, M.,
823　　Zeng, L., Zhu, T., Zhang, Y., and Wahner, A.: Maximum efficiency in the hydroxyl-
824　　radical-based self-cleansing of the troposphere, Nature Geoscience 7, 559–563,
825　　doi:10.1038/ngeo2199, 2014.

826 Sander, S. P., Abbatt, J., Barker, J. R., Burkholder, J. B., Friedl, R. R., Golden, D. M., Huie,
827　　R. E., Kolb, C. E., Kurylo, M. J., Moortgat, G. K., Orkin, V. L. and Wine, P. H.: Chemical
828　　Kinetics and Photochemical Data for Use in Atmospheric Studies, Evaluation No. 17, JPL
829　　Publication 10-6, Jet Propulsion Laboratory, Pasadena, available at:
830　　http://jpldataeval.jpl.nasa.gov (last access: October 27, 2015), 2011.

831 Schneising, O., Buchwitz, M., Burrows, J. P., Bovensmann, H., Bergamaschi, P., and Peters,
832　　W.: Three years of greenhouse gas column-averaged dry air mole fractions retrieved from
833　　satel- lite − Part 2: Methane, Atmos. Chem. Phys., 9, 443–465, doi:10.5194/acp-9-443-
834　　2009, 2009.

835 Schneising, O., Buchwitz, M., Reuter, M., Heymann, J., Bovens- mann, H., and Burrows, J.
836　　P.: Long-term analysis of car- bon dioxide and methane column-averaged mole fractions
837　　re- trieved from SCIAMACHY, Atmos. Chem. Phys., 11, 2863− 2880, doi:10.5194/acp-
838　　11-2863-2011, 2011.

839 Schultz, M., S. Rast, M. van het Bolscher, T. Pulles, R. Brand, J. Pereira, B. Mota, A.
840　　Spessa, S. Dalsøren, T. van Nojie, S. Szopa, Emission data sets and methodologies for
841　　estimating emissions, RETRO project report D1-6, Hamburg, 26 Feb 2007, available at:
842　　http://gcmd.gsfc.nasa.gov/records/GCMD_GEIA_RETRO.html (last access: October 27,
843　　2015), 2007.

844 Shindell, D. T., Faluvegi, G., Stevenson, D. S., Krol, M. C., Emmons, L. K., Lamarque, J.-F.,
845　　Petron, G., Dentener, F. J., Ellingsne, K., Schultz, M. G., Wild, O., Amann, M., Atherton,
846　　C. S., Bergmann, D. J., Bey, I., Butler, T., Cofala, J., Collins, W. J., Derwent, R. G.,
847　　Doherty, R. M., Drevet, J., Eskes, H. J., Fiore, A. M., Gauss, M., Hauglustaine, D. A.,
848　　Horowitz, L.W., Isaksen, I. S. A., Lawrence, M. G., Montanaro, V., M¨uller, J.-F., Pitari,
849　　G., Prather, M. J., Pyle, J. A., Rast, S., Rodriguez, J. M., Sanderson, M. G., Savage, N. H.,
850　　Strahan, S. E., Sudo, K., Szopa, S., Unger, N., van Noije, T. P. C., and Zeng, G.:

Multimodel simulations of carbon monoxide: Comparison with observations and projected near-future changes, J. Geophys. Res., 111, D19306, doi:10.1029/2006JD007100, 2006.

Spivakovsky, C, Wofsy, S., and Prather, M.: A numerical method for the parameterization of atmospheric chemistry: Computation of tropospheric OH, J. Geophys. Res., 95, 18,433-18,439, 1990a.

Spivakovsky, C.M., Yevich, R., Logan, J.A., Wofsy, S.C., McElroy, M.B., and Prather, M.J., Tropospheric OH in a three-dimensional chemical tracer model: An assessment based on observations of CH_3CC1_3, J. Geophys. Res., 95, 18,441-18,471, doi:10.1029/JD095iD11p18441, 1990b.

Spivakovsky, C M., Logan, J A., Montzka, S A., Balkanski, Y J. Foreman-Fowler, M., Jones, D B A., Horowitz, L W., Fusco, A C., Brenninkmeijer, C A M., Prather, M J., Wofsy, S C., and McElroy, M B.: Three-dimensional climatological distribution of tropospheric OH: Update and evaluation, J. Geophys. Res., 105, D7, 8931–8980, doi:10.1029/1999JD901006, 2000.

Stone, D., L.K. Whalley, D.E. Heard.: Tropospheric OH and HO_2 radicals: field measurements and model comparisons. Chemical Society Reviews, 41:19, 6348, doi:10.1039/c2cs35140d, 2012.

Strahan, S.E., B.N. Duncan and P. Hoor, Observationally-derived diagnostics of transport in the lowermost stratosphere and their application to the GMI chemistry transport model, Atmos. Chem. Phys., 7, 2435-2445, 2007.

Strode, S. A., Duncan, B. N., Yegorova, E. A., Kouatchou, J., Ziemke, J. R., and Douglass, A. R.: Implications of model bias in carbon monoxide for methane lifetime, Atmos. Chem. Phys. Discuss., 15, 20305-20348, doi:10.5194/acpd-15-20305-2015, 2015.

Voulgarakis, A., Naik, V., Lamarque, J.-F., Shindell, D. T., Young, P. J., Prather, M. J., Wild, O., Field, R. D., Bergmann, D., Cameron-Smith, P., Cionni, I., Collins, W. J., Dalsøren, S. B., Doherty, R. M., Eyring, V., Faluvegi, G., Folberth, G. A., Horowitz, L. W., Josse, B., MacKenzie, I. A., Nagashima, T., Plummer, D. A., Righi, M., Rumbold, S. T., Stevenson, D. S., Strode, S. A., Sudo, K., Szopa, S., and Zeng, G.: Analysis of present day and future OH and methane lifetime in the ACCMIP simulations, Atmos. Chem. Phys., 13, 2563-2587, doi:10.5194/acp-13-2563-2013, 2013.

Voulgarakis, A., M. E. Marlier, G. Faluvegi, D. T. Shindell, K. Tsigaridis, and S. Mangeon, Interannual variability of tropospheric trace gases and aerosols: The role of biomass burning emissions, J. Geophys. Res. Atmos., 120, 7157–7173, doi:10.1002/2014JD022926, 2015.

Wang, J. S., Logan, J. A., McElroy, M. B., Duncan, B. N., Megretskaia, I. A., Yantosca, R. M.: A 3-D model analysis of the slowdown and interannual variability in the methane growth rate from 1988 to 1997, Global Biogeochemical Cycles, 18, GB3011, doi:10.1029/2003GB002180, 2004.

Wang, J. S., McElroy, M. B., Logan, J. A., Palmer, P. I., Chameides, W. L., Wang, Y., and Megretskaia, I. A.: A quantitative assessment of uncertainties affecting estimates of global mean OH derived from methyl chloroform observations, J. Geophys. Res., 113, D12302, doi:10.1029/2007JD008496, 2008.

Wainwright, C. D., Pierce, J. R., Liggio, J., Strawbridge, K. B., Macdonald, A. M., and Leaitch, R. W.: The effect of model spatial resolution on Secondary Organic Aerosol

895   predictions: a case study at Whistler, BC, Canada, Atmos. Chem. Phys., 12, 10911-10923,
896   doi:10.5194/acp-12-10911-2012, 2012.

897   Wild, O., and Palmer, P. I.: How sensitive is tropospheric oxidation to anthropogenic
898   emissions?, Geophys. Res. Lett., 35, L22802, doi:10.1029/2008GL035718, 2008.

899   Wolter, K., and M. S. Timlin, El Niño/Southern Oscillation behaviour since 1871 as
900   diagnosed in an extended multivariate ENSO index (MEI.ext). Intl. J. Climatology, 31,
901   1074-1087, DOI: 10.1002/joc.2336, 2011.

902   Worden, H. M., Deeter, M. N., Edwards, D. P., Gille, J. C., Drummond, J. R., and Nédélec,
903   P.: Observations of near-surface carbon monoxide from space using MOPITT
904   multispectral retrievals, J. Geophys., Res., 115, D18314, doi:10.1029/2010JD014242,
905   2010.

906

907 Table 1: Reference Scenario (*Base*) Description

AGCM Input	Description[a]
Dynamics	Model dynamics are constrained by sea surface temperatures and sea ice concentrations from the Community Climate System Model (http://www.cesm.ucar.edu/models/ccsm4.0/, CCSM-4) through 2005 and from 2006 to 2007 from CCSM-4 with Representative Concentration Pathways (RCP 6.0, Fujino et al. (2006); Hijioka et al. (2008)). The methane tracer is radiatively inactive and archived annually-varying methane fields used in the radiation code; our aim is reproduce the same meteorology in all simulations so as to more cleanly isolate the impact of the causal factors on methane, CO, and OH trends and variations.
Parameterization of OH Input	
Chemical Variables	Nitrogen oxides (as a family), ozone, overhead ozone column, and various VOCs are monthly, archived fields for 2000 and are repeated for each year of the *Base* simulation; these fields were taken from a one year (2000) GEOS-5 AGCM simulation, which was part of the ACCMIP study (Lamarque et al., 2013), with a full-representation of ozone-NO_x-VOC photochemistry (Duncan et al., 2007b; Strahan et al., 2007) and emissions of NO_x, VOCs, and species important to the stratospheric ozone layer (e.g., N_2O, HFCs, CFCs).
Meteorological Variables	Pressure, temperature, cloud albedo and water vapor are taken from the AGCM as the simulation progresses.
Emissions[b]	
Methane	Annually-repeating natural (e.g., wetlands, biomass burning) and annually-varying anthropogenic emissions (EDGAR 3.2, TransCom CTL scenario) are described in Patra et al. (2011).
CO	Annually-repeating emissions representative for year 2000 time slice of the ACCMIP (Lamarque et al., 2013; Strode et al., 2015).
Methane Oxidation	
Troposphere	CH_4 + OH → αCO: tropospheric OH calculated by parameterization of OH. CO yield (α) = 1 (Duncan et al., 2007a).
Stratosphere	Calculated based on its reaction with OH, Cl and O^1D from archived monthly fields from one year of an AGCM simulation.
VOC Oxidation[b]	VOC + OH → αCO; CO yield (α) varies with VOC (Duncan et al., 2007b). Isoprene + OH → αCO, where CO yield (α) varies with [NO_x] (Duncan et al., 2007a).

908 [a]All scenarios are for 1988-2007. We use the methane initial condition of 1655 ppb by January 1988 at the GMD South Pole (SPO) station,
909 (Patra et al., 2011, TransCom protocolv7), which was reached after a 12-year model spin up; results are thus considered valid from January 1,
910 1988.
911 [b]Only methane and CO are treated as emission fluxes. The source of CO via VOC oxidation is calculated using archived, 3d fields from a GEOS-5 AGCM full chemistry
912 simulation. Figures S1 and S2 show the methane and CO fluxes, respectively, used in all scenarios.
913

914   Table 2: Description of Simulation Scenarios

Model Scenario	Relation to Other Scenarios	Purpose of Scenario
1. *Base*	Table 1.	Reference scenario
2. $E_{CH4}Vary$ *Base* + all methane source types varying annually	Same as *Base*, except that the "EXTRA" methane emission scenario is used (Patra et al., 2011). The primary difference between the CTL and EXTRA scenarios is that the CTL emissions are composed of repeating annual cycles of all source types, except for anthropogenic emissions which varies from year-to-year, while the EXTRA emission scenario has all source types (e.g., biomass burning, wetlands, rice paddies, etc.) varying annually (Fig. S 1)).	To understand the influence of interannual variations in natural sources of methane on the trends and variations of model OH and observed methane and CO distributions. Wetlands are the largest single source of methane and the largest source of interannual variations (e.g., Patra et al., 2011; Voulgarakis et al., 2015).
3. $BBE_{CO}Vary$ *Base* + BB CO emissions *varying annually*	Same as *Base*, except CO emissions from biomass burning (BB) annually vary. Emissions are from the REanalysis of the TROpospheric chemical composition (RETRO v2.0, Schultz et. al., 2007) emission inventory for 1988-1996 and the Global Fire Emissions Database (GFEDv3.1, Giglio et al., 2010; Randerson et al., 2013) for years 1997-2007.	To understand the influence of interannual variations in the biomass burning source of CO (Fig. S 2). From 1988-2007, there were several large events, such as in Indonesia in 1997 [Duncan et al., 2003a] and 2006 and worldwide in 1998 [Duncan et al., 2003b].
4. $FFBBE_{CO}Vary$ *Base* + FF and BB CO emissions varying annually	Same as $BBE_{CO}Vary$, except CO emissions from fossil fuels annually vary. Anthropogenic emissions are from the Emission Database for Global Atmospheric Research (EDGARv4.2) for 1988-2007.	To understand the combined influence of interannual variations in the anthropogenic and biomass burning sources of CO.
5. $OH_{Input}Vary$ *Base* + parameterization of OH chemical variables varying annually	Same as *Base*, except the monthly, archived chemical variables used as input to the parameterization of OH are annually varying. Taken from the same GEOS-5 AGCM simulation as in *Base* scenario with a full-representation of ozone-NO_x-VOC photochemistry and annually varying anthropogenic and biogenic emissions of NO_x, VOCs, and species important to the stratospheric ozone layer (e.g., N_2O, HFCs, CFCs) (Strahan et al., 2007; Duncan et al., 2007b; Oman et al., 2011).	To understand the influence of interannual variations in other factors that affect OH. These factors include the overhead ozone column, NO_x and anthropogenic VOCs.
6. *AllVary* *Base* + $E_{CH4}Vary$ + $FFBBE_{CO}Vary$ + $OH_{Input}Vary$	Annually varying methane and CO emissions from all sources and annually-varying factors that influence OH.	To understand the combined influence of annually-varying 1) CO emissions from fossil fuel and biomass burning, 2) effects of NO_x and VOCs on OH, and 3) methane emissions from all sources.

915

916 Table 3: Data Used In Model Evaluation of Methane, CO, and OH

Data	Species	Quantity	Time Range	Reference
NOAA ESRL Global Monitoring Division (GMD) surface data	CO, methane	mixing ratio (ppbv)	1980-present	Novelli et al., 1992, 1998; Dlugokencky et al., 2010, 2014.
Envisat SCanning Imaging Absorption spectroMeter for Atmospheric CHartographY (SCIAMACHY)[a]	methane	atmospheric column (molec/cm^2)	2003-2005	Bovensmann et al., 1999; Schneising et al., 2009; Schneising et al., 2011; Frankenberg et al., 2011
Terra Measurement of Pollution In The Troposphere (MOPITT) Instrument[b]	CO	atmospheric column (molec/cm^2)	1999-present	Worden, 2010; Deeter et al., 2012; Deeter, 2013.
Aura Tropospheric Emission Spectrometer (TES)/Microwave Limb Sounder (MLS) Joint Product	CO	mixing ratio (ppbv)	8/2004-10/2012	Luo et al., 2013
NOAA surface network	MCF	OH interannual variability (IAV)[c]	1997-2007	Montzka et al., 2011

917 [a]We use version 3.7 gridded product of the column-averaged methane dry mole fraction (Schneising et al., 2009; http://www.iup.uni-
918 bremen.de/sciamachy/NIR_NADIR_WFM_DOAS/products).The methane data since November 2005 are considered to be of reduced quality (in comparison to data from
919 2003-October 2005) due to detector degradation in the spectral range used for the methane column retrieval (Schneising et al., 2011; Frankenberg et al., 2011).
920 [b]We use the gridded monthly CO retrievals (thermal infrared radiances) V006 L3 product (http://eosweb.larc.nasa.gov)
921 [c]There are only very sparse and uncertain direct observations (e.g., Stone et al., 2012).
922

923 Table 4: list of the correlation parameters of the different model scenarios and the monthly

924 GMD measurements for the simulation period (1988-2007)

Scenario	ALT[a]		BRW		NWR		MLO		RPB		SPO	
	S*	R[2]**	S	R[2]	S	R[2]	S	R[2]	S	R[2]	S	R[2]
CH$_4$ data												
Base	0.56	0.66	0.57	0.60	0.76	0.64	0.76	0.58	0.68	0.82	0.79	0.91
E$_{CH4}$Vary	0.74	0.68	0.74	0.56	0.74	0.63	0.79	0.57	0.71	0.72	0.82	0.89
BBE$_{CO}$Vary	0.82	0.68	0.84	0.66	1.03	0.76	1.07	0.72	1.00	0.84	1.07	0.93
FFBBE$_{CO}$Vary	0.58	0.54	0.56	0.46	0.74	0.54	0.77	0.52	0.66	0.64	0.79	0.81
OH$_{input}$Vary	0.53	0.63	0.53	0.56	0.71	0.60	0.70	0.56	0.62	0.78	0.74	0.90
AllVary	0.69	0.49	0.68	0.40	0.64	0.45	0.70	0.43	0.62	0.47	0.76	0.73
CO data												
Base	0.74	0.79	0.70	0.75	0.83	0.57	0.98	0.71	0.74	0.68	0.88	0.82
E$_{CH4}$Vary	0.74	0.79	0.70	0.75	0.82	0.57	0.98	0.71	0.73	0.68	0.87	0.82
BBE$_{CO}$Vary	0.81	0.86	0.74	0.73	0.84	0.57	1.01	0.74	0.82	0.68	0.79	0.64
FFBBE$_{CO}$Vary	0.92	0.88	0.97	0.87	0.84	0.42	0.89	0.70	0.83	0.70	0.81	0.63
OH$_{input}$Vary	0.74	0.81	0.71	0.77	0.81	0.56	0.93	0.71	0.67	0.66	0.92	0.85
AllVary	0.90	0.88	0.96	0.85	0.80	0.37	0.82	0.68	0.77	0.67	0.84	0.68

925 [a]GMD stations shown include Alert, Canada (ALT, 82ºN, 62ºW), Point Barrow, USA (BRW, 71ºN, 156ºW), Niwot Ridge, USA (NWR, 40ºN, 105ºW),

926 Mauna Loa, Hawaii, USA (MLO, 20ºN, 155ºW), Ragged Point, Barbados (RPB, 13ºN, 59ºW), and South Pole,

927 Antarctica (SPO, 90ºS, 25ºW).

928 *: "S" refers to the correlation slope (dy/dx) of the simulation/measurement comparison.

929 **: "R[2]" refers to the correlation coefficient.

930
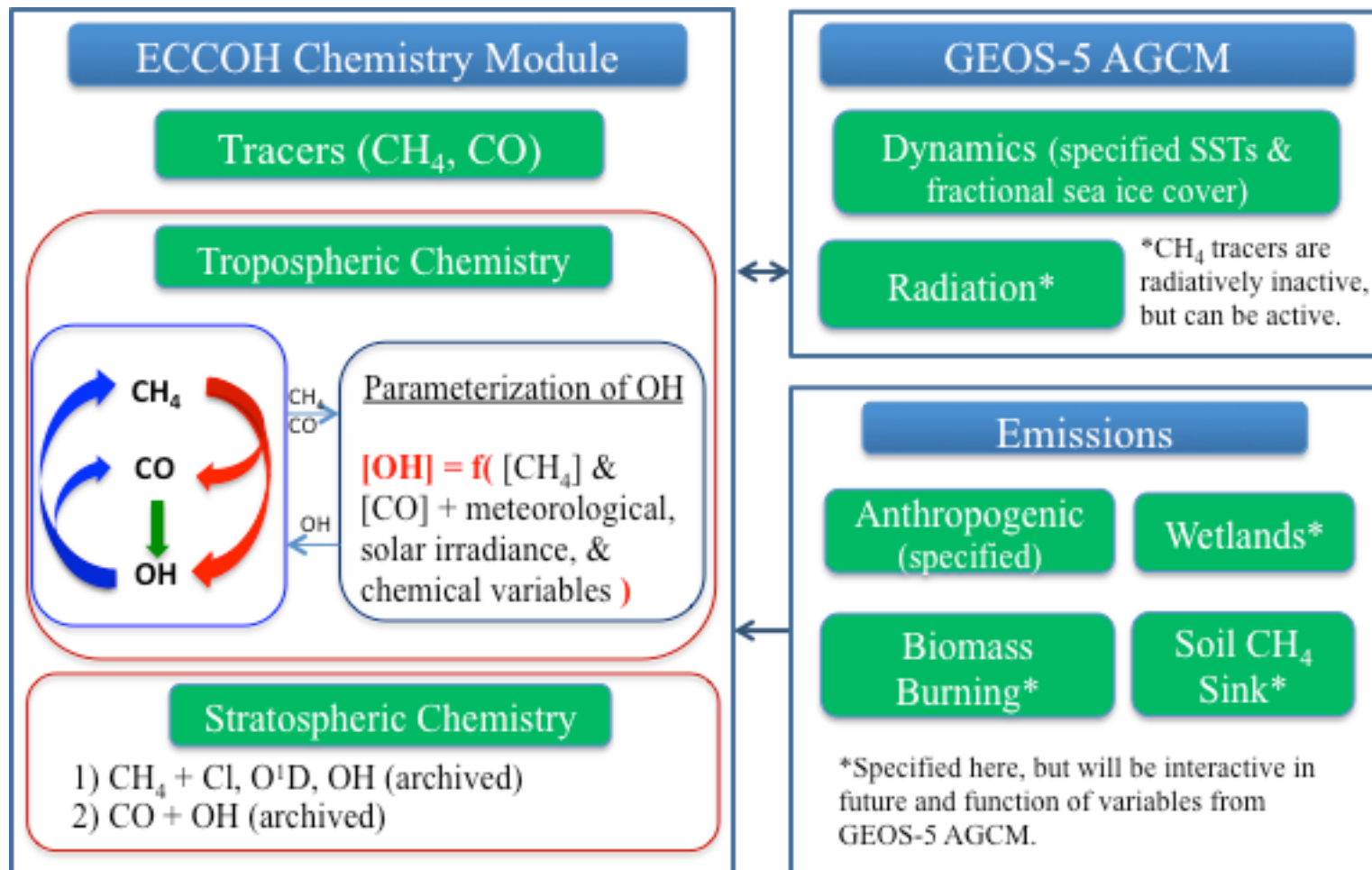
Fig. 1: Schematic representation of the implementation of the ECCOH module within the GEOS-5 AGCM.
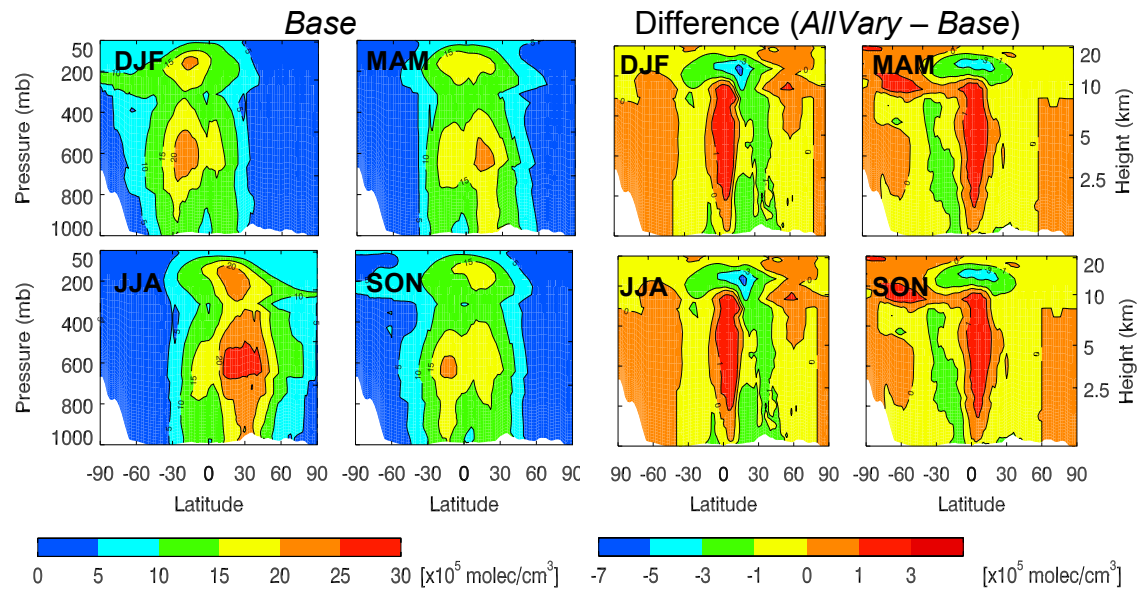
Fig. 2: Seasonal zonal mean (1988-2007) of OH (x10^{5}molecules/cm^3) for the *Base* scenario (left 4 panels) and the difference (*AllVary-Base*, right 4 panels) for December-February (DJF), March-May (MAM), June-August (JJA) and September-November (SON).
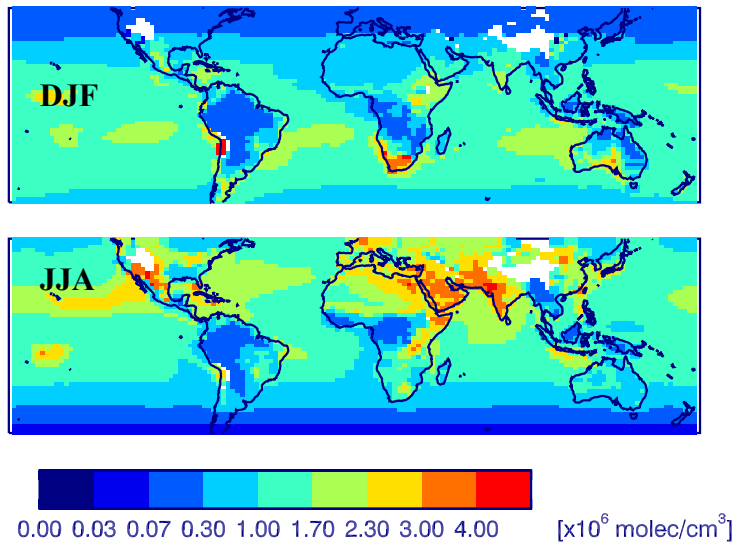
Fig. 3: Seasonal mean (1988-2007) OH (x10^{6} molecules/cm^{3}) for the *Base* scenario for December- February (DJF) and June-August (JJA) at 850 mb.
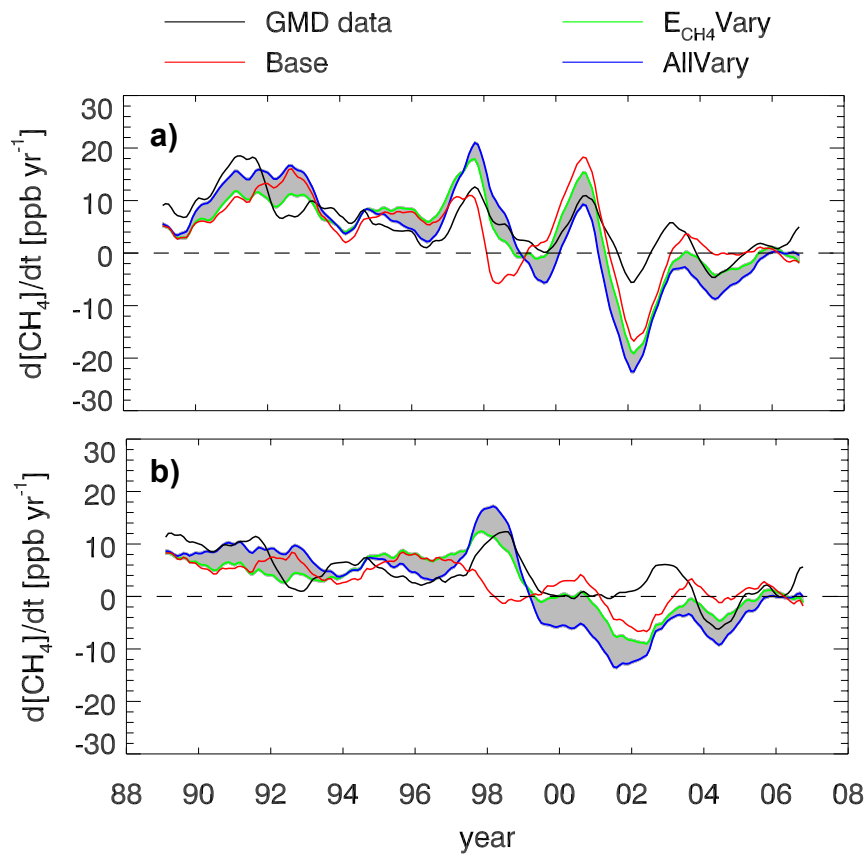
Fig. 4: a) 12-month running mean atmospheric growth rate of methane (ppbv yr^{-1}) for the average of 92 GMD stations and from model output for several scenarios averaged for those station locations. The shaded area is the difference between the $E_{CH4}Vary$ and *AllVary* scenarios, which indicates the total contribution of nonlinear feedbacks (i.e., from variations of CO emissions and variables input to the parameterization of OH) of the CH$_4$-CO-OH system to methane's growth rate. b) Same as a) but for the average of 17 GMD stations, which covers 100% of the simulation period. Refer to Fig. S 4 to Fig. S 7 for methane's growth rate from other scenarios.
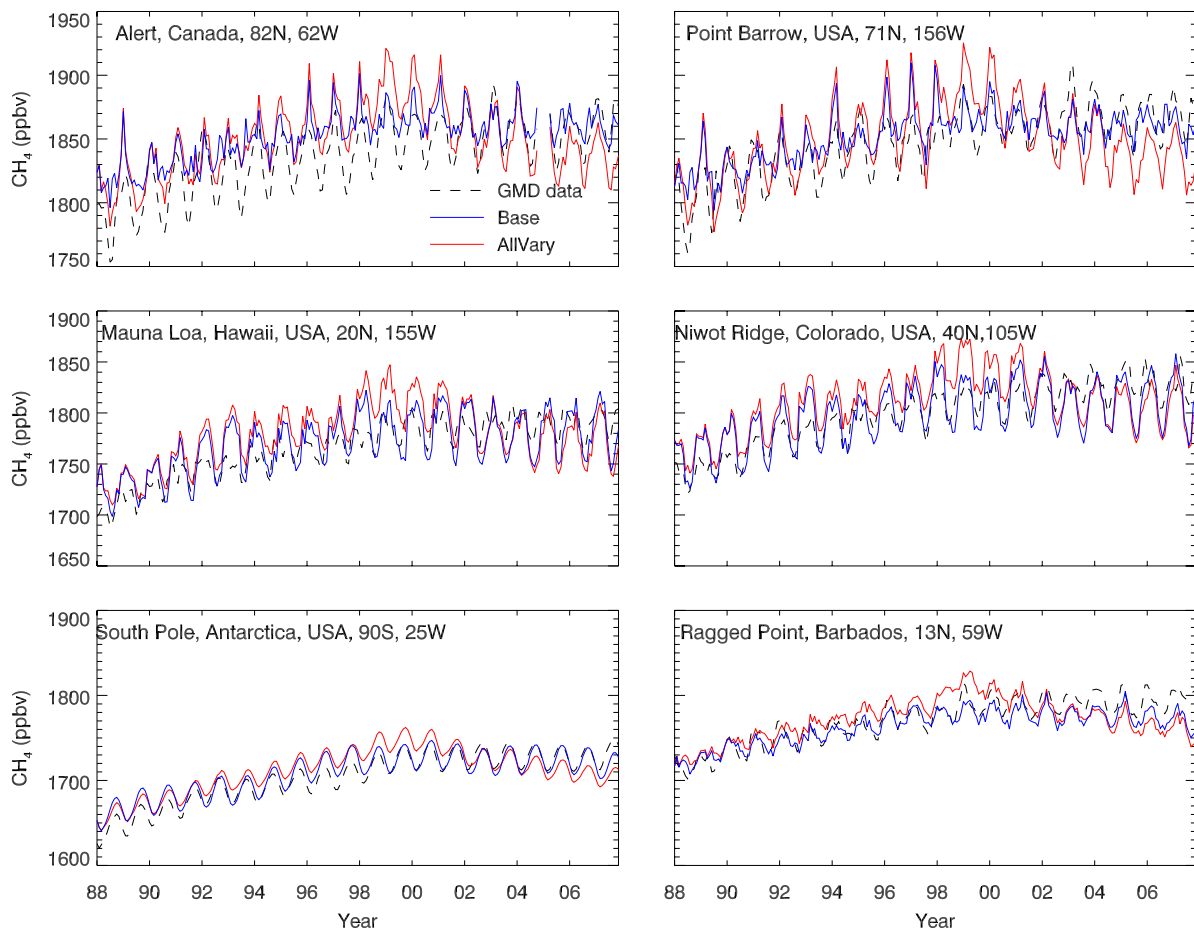
Fig. 5: Monthly methane (ppbv) from the *Base* and *AllVary* scenarios and observations from six GMD stations. Similar plots for the other scenarios are given in Fig. S 8 to Fig. S 11.
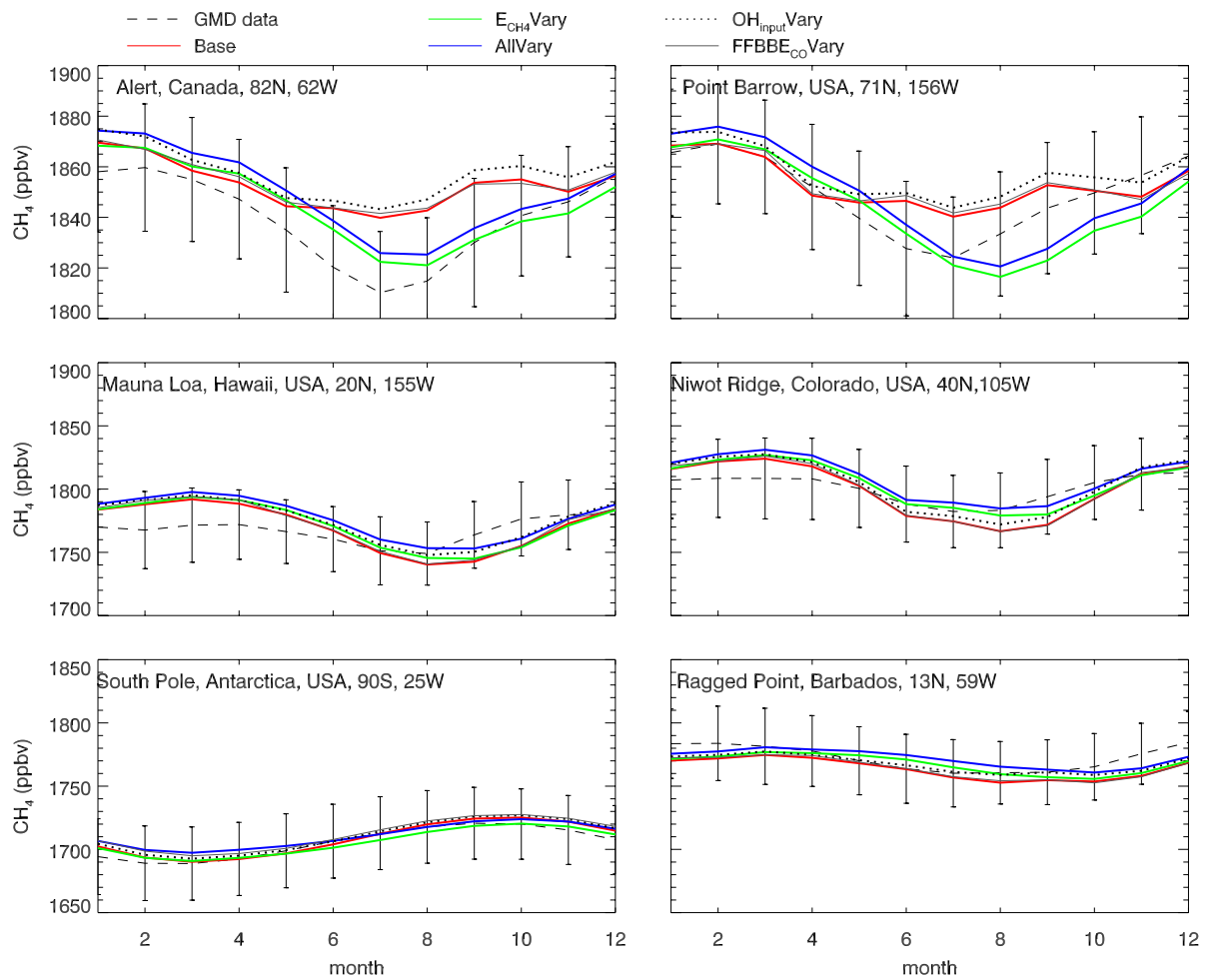
Fig. 6: Monthly methane (ppbv) averaged over 1988-2007 for several scenarios and observations at six GMD stations. Vertical lines represent the standard deviation of the observed annual mean.
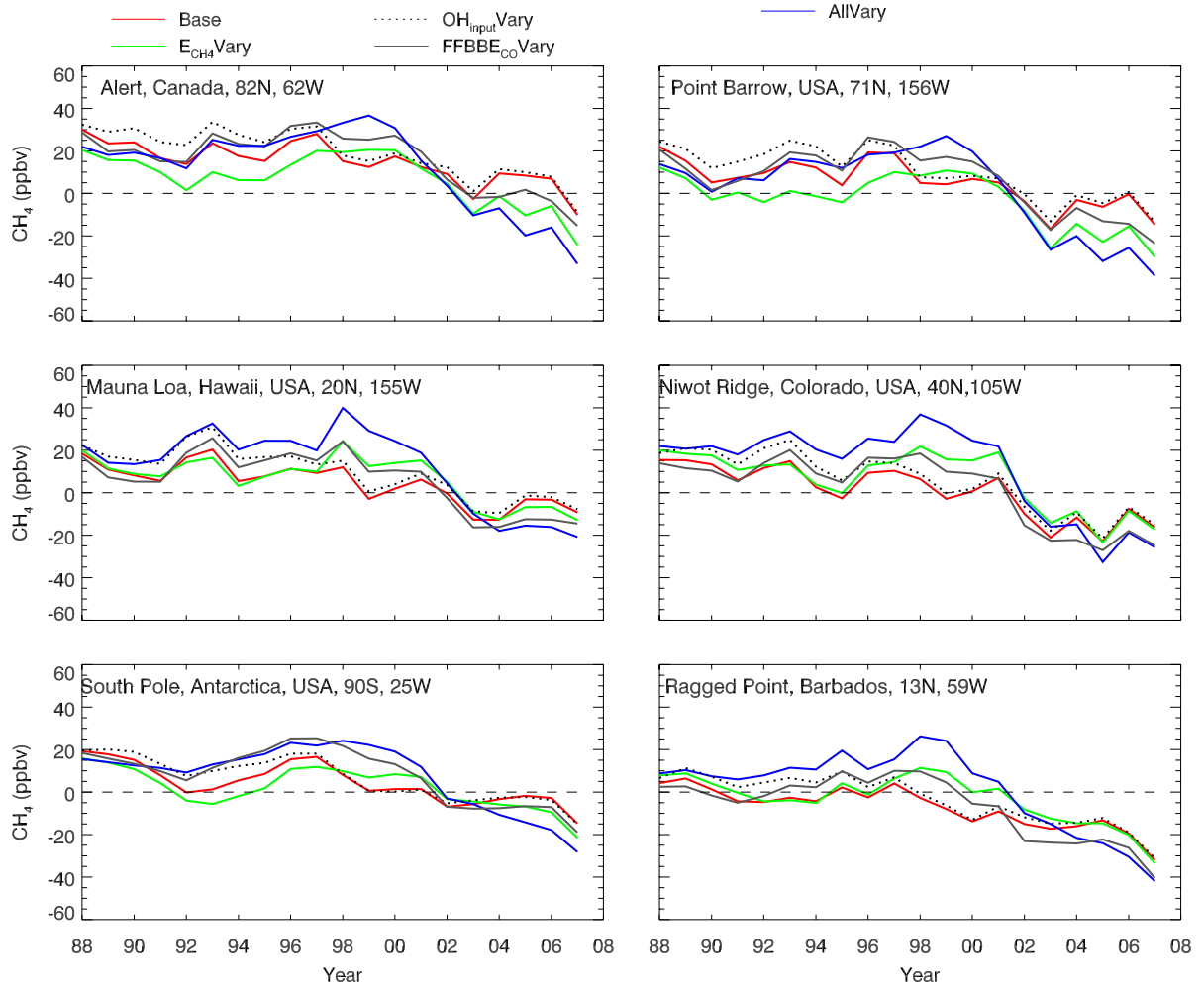
Fig. 7: Annual methane deviation (ppbv; simulated-measured) for several scenarios and observations at six GMD stations.

Base — **Relative difference [%]**

DJF

JJA

1640 1680 1720 1740 1760 1780 1800 1820 1840 1880 [ppb]

-20   -5   -1   1   5   20   [%]
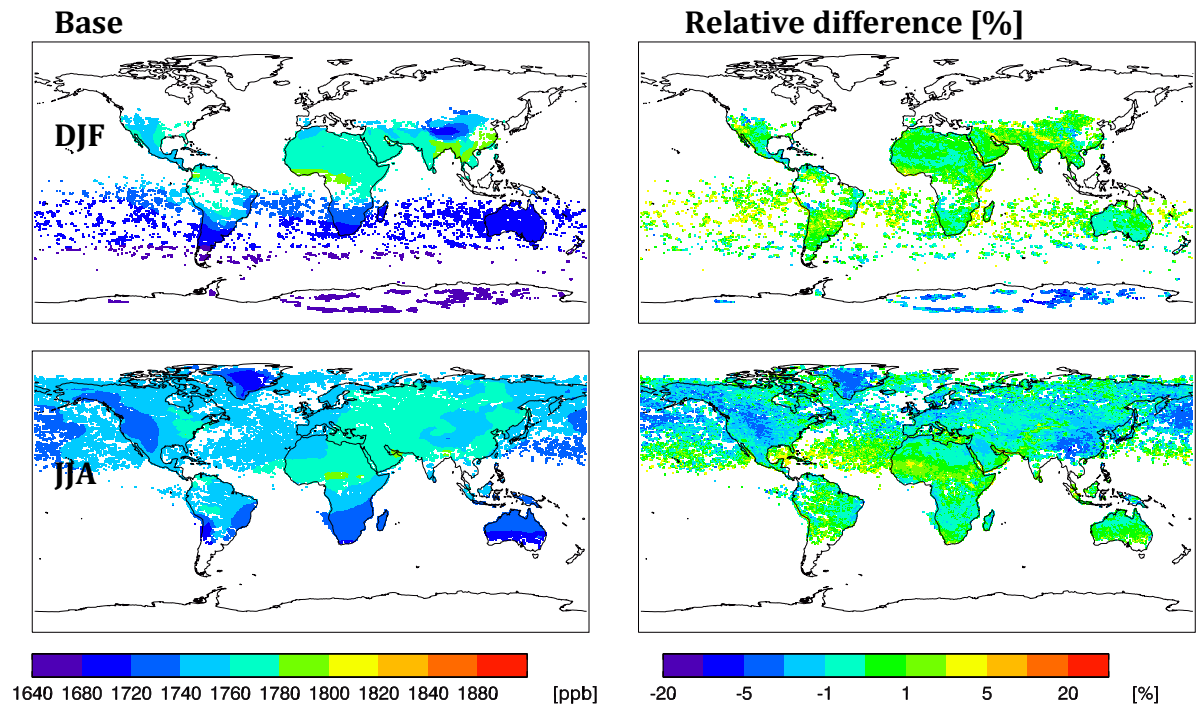
Fig. 8: Seasonal mean (2004) methane dry column (ppbv; left column) from the *Base* scenario and the relative difference (%, (*Base*-observations)/observations; right column) with SCIAMACHY data. Simulated methane levels are gridded to the spatial resolution of the SCIAMACHY data.
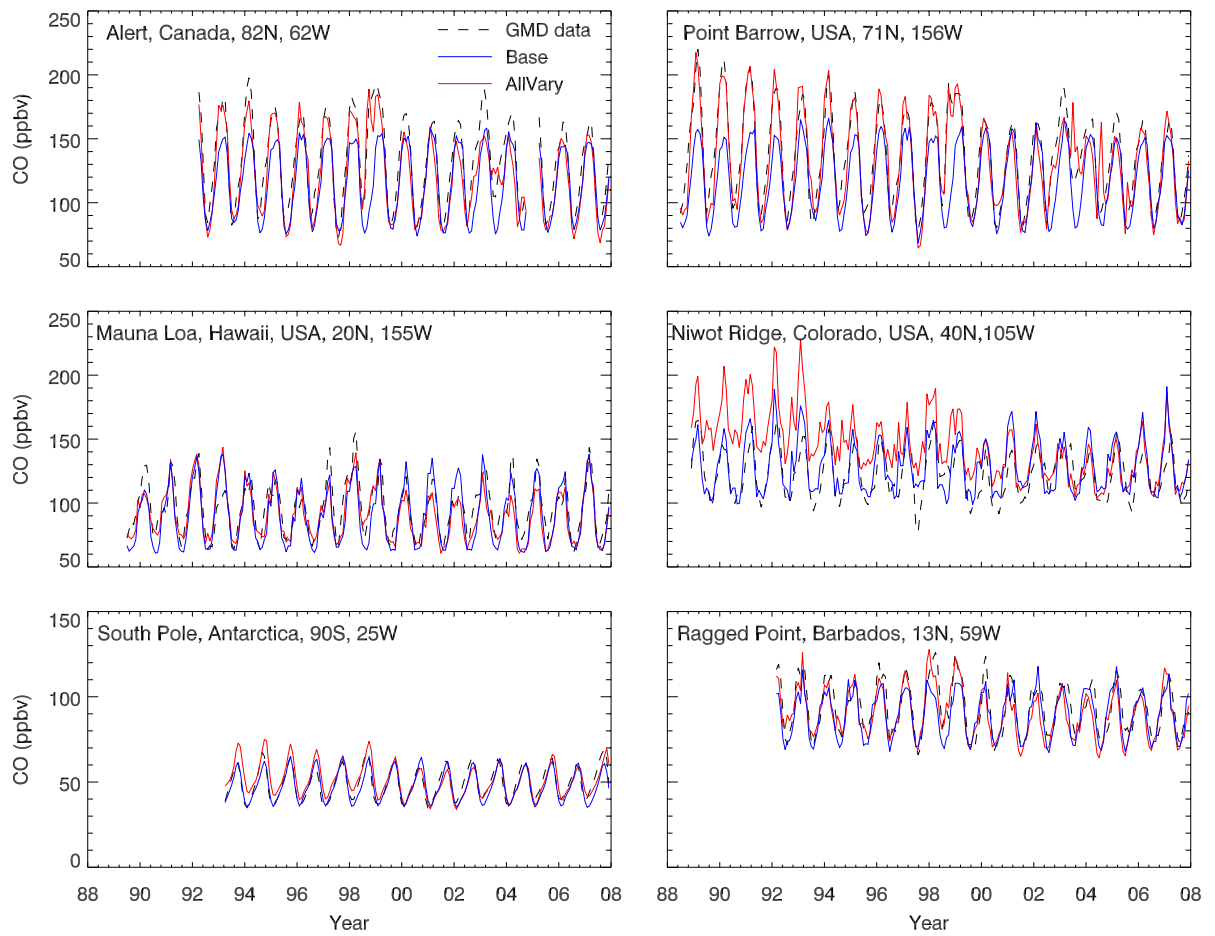
Fig. 9: Monthly CO (ppbv) from the *Base* and *AllVary* scenarios and observations from six GMD stations. Similar plots for the other scenarios are given in Fig. S13 to Fig. S16.
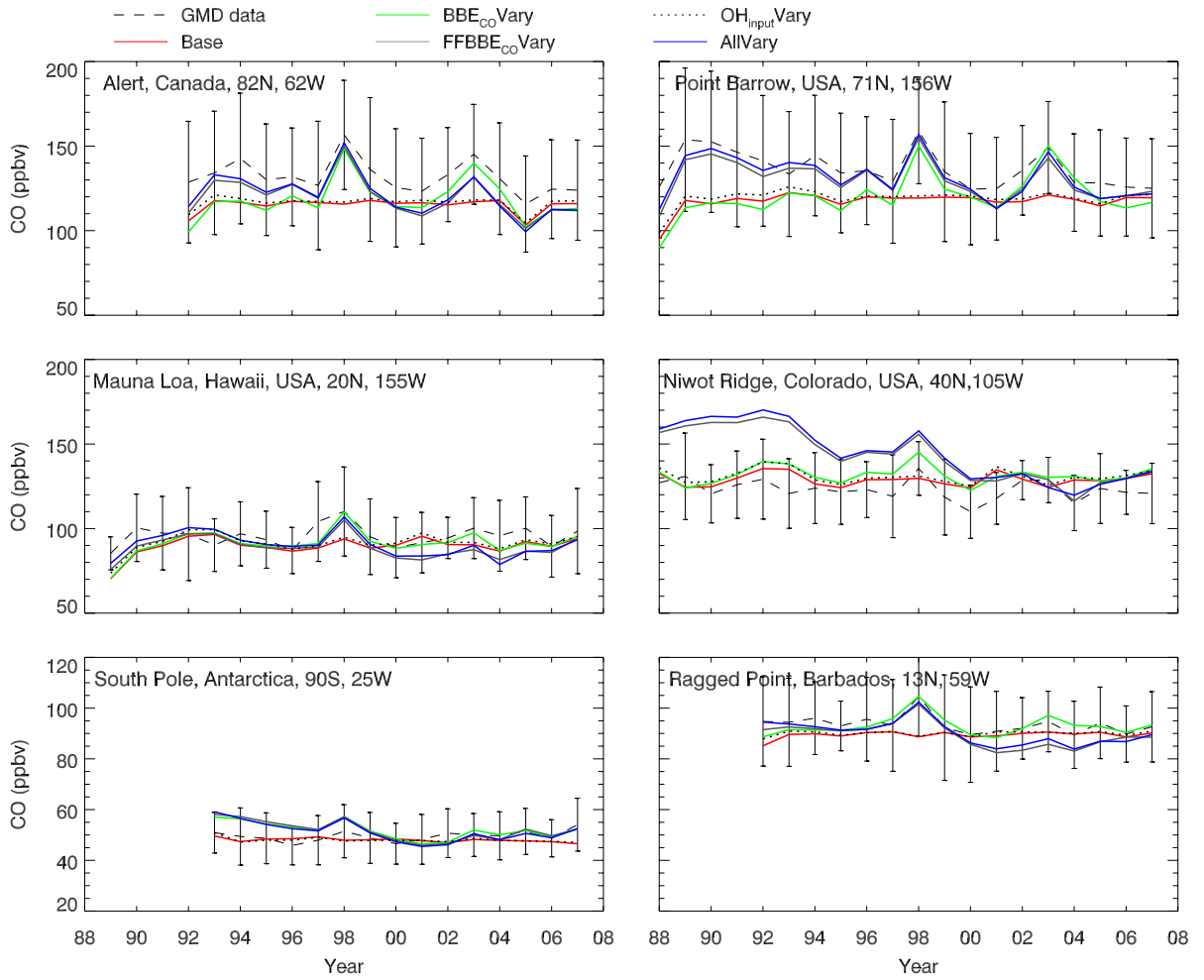
Fig. 10: Annual mean CO (ppbv) from several scenarios and observations at six GMD stations. Vertical lines represent the standard deviation of the observed annual mean.
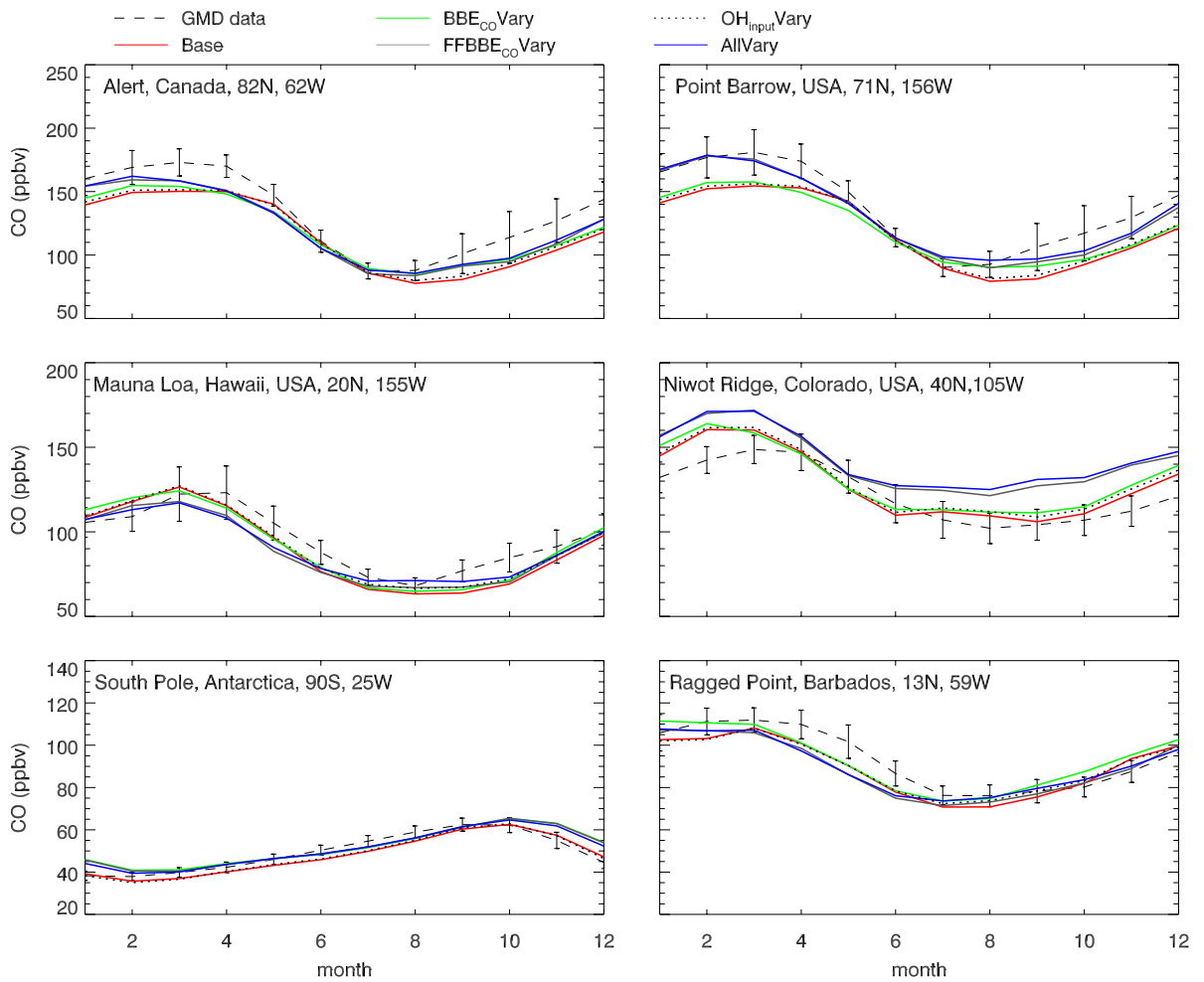
Fig. 11: Monthly CO (ppbv) averaged over 1998-2007 for several scenarios and observations at six GMD stations. Vertical lines represent the standard deviation of the observed monthly mean.
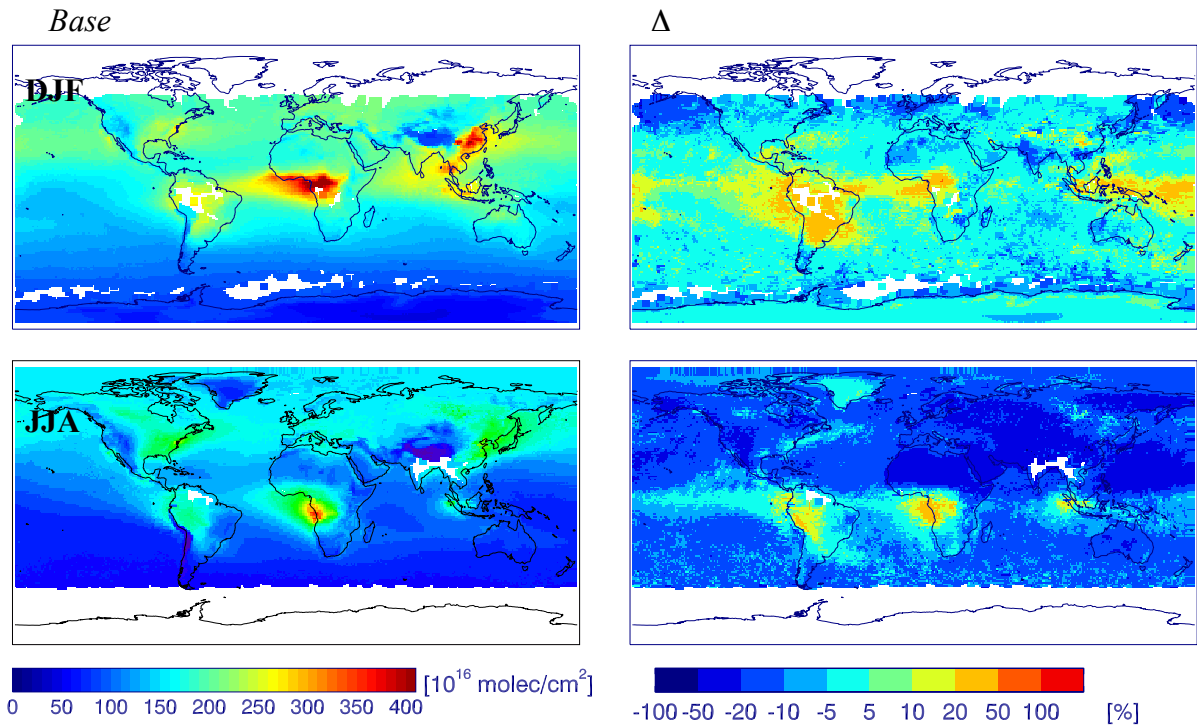
Fig. 12: Seasonal mean (2006-2007) CO columns (x10^{16} molecules/cm^2) from the *Base* scenario (left column) and the relative difference (%; (*Base*-observations)/observations; right column) with MOPITT data.
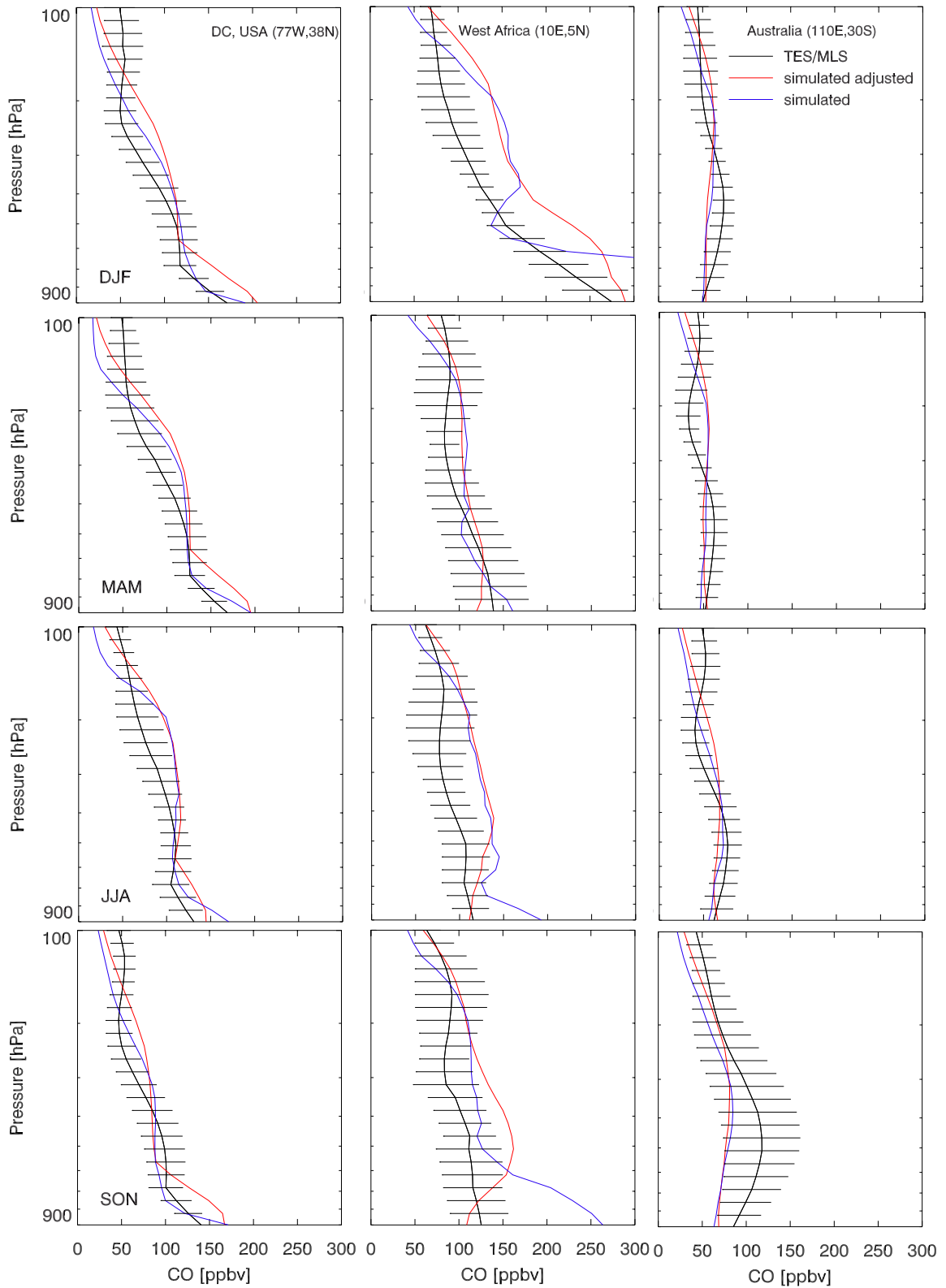
Fig. 13: Seasonal mean (2006-2007) CO vertical profiles (ppbv) over select locations of TES/MLS data, the *Base* scenario ('simulated'), and the *Base* scenario adjusted with averaging kernels ('simulated adjusted'). The horizontal bars represent the standard deviation of the individual overpasses used to create the seasonal mean.
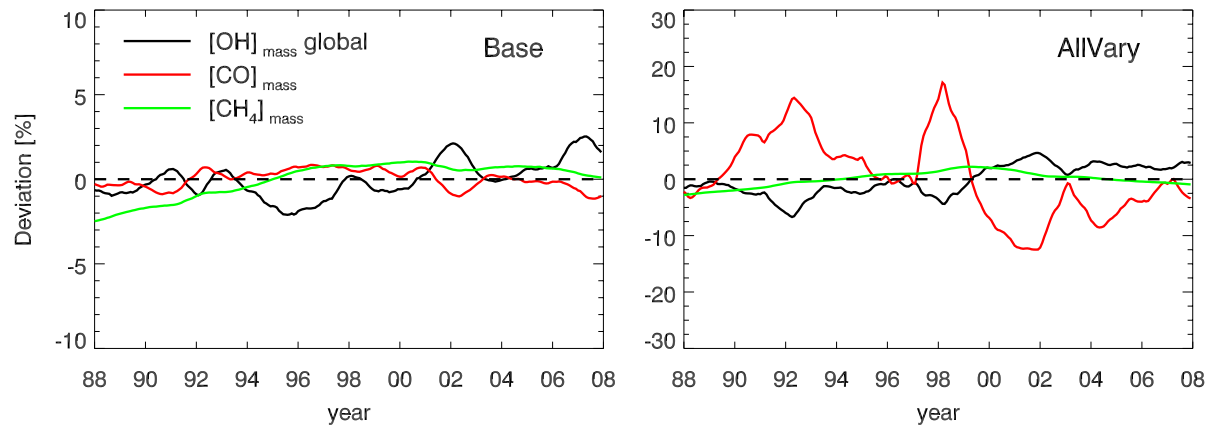
Fig. 14: Deviations of tropospheric, mass-weighted OH, CO and methane (12 month running mean) from the *Base* (left) and *AllVary* (right) scenarios. Note the different scales of the y-axes.
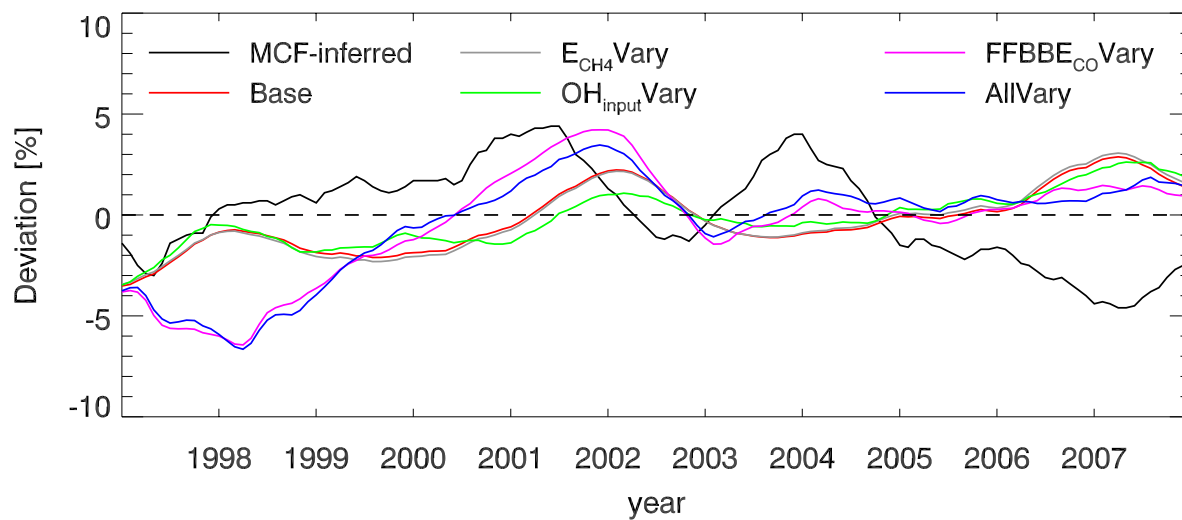
Fig. 15: Deviations (%) of the global, mass-weighted, pseudo first order rate constant (k') of the reaction of OH with MCF-inferred from MCF measurements (black; adapted from Montzka et al., 2011) and from several scenarios.
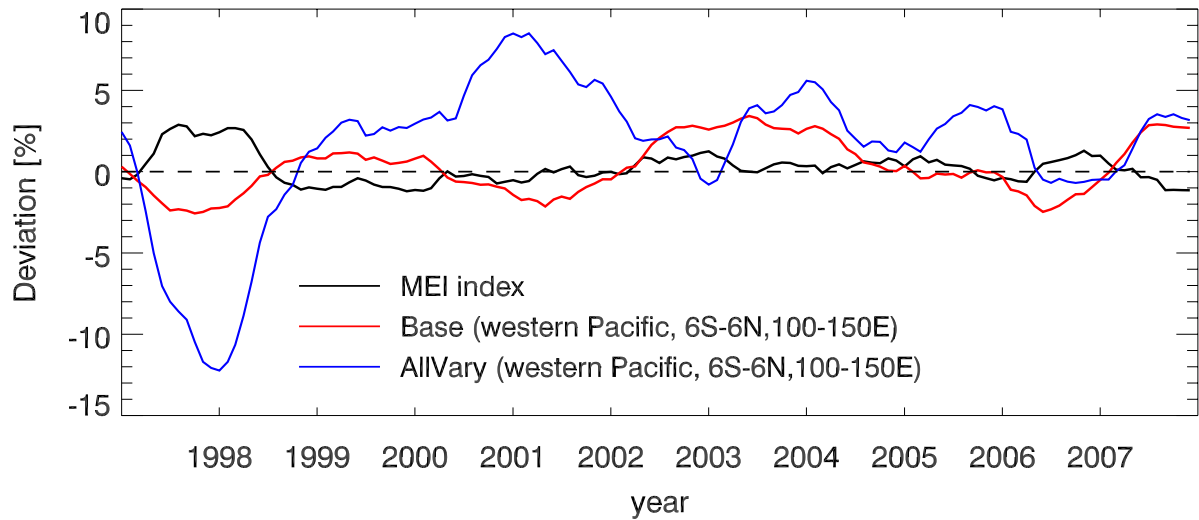
Fig. 16: Deviation (%) of global, mass-weighted OH from various scenarios and the Multivarient ENSO Index (MEI). The lines are 12-month running means. Positive values of MEI indicate El Niño conditions and negative values indicate La Niña conditions. The correlation coefficient (R^2) for the *Base* scenario vs the MEI index is 0.20 while for the *AllVary* scenario is 0.59.
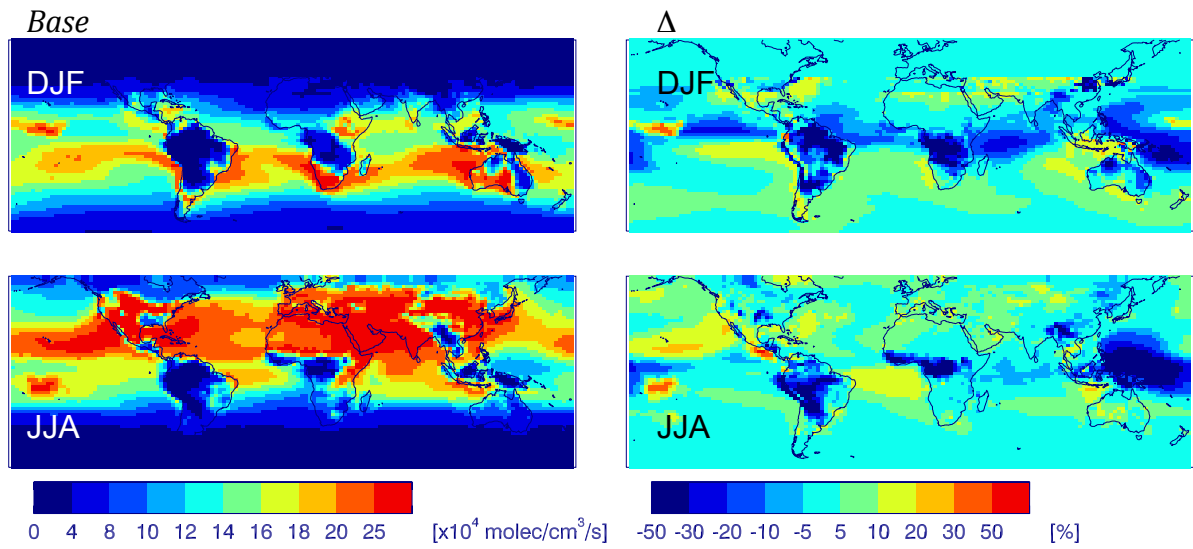
Fig. 17: Seasonal mean (1988-2007), mass-weighted tropospheric methane loss rate (left column; x10^4 molecules/cm^3/s) with relative difference with the *AllVary* scenario ((*Base-AllVary)/Base*; right column).
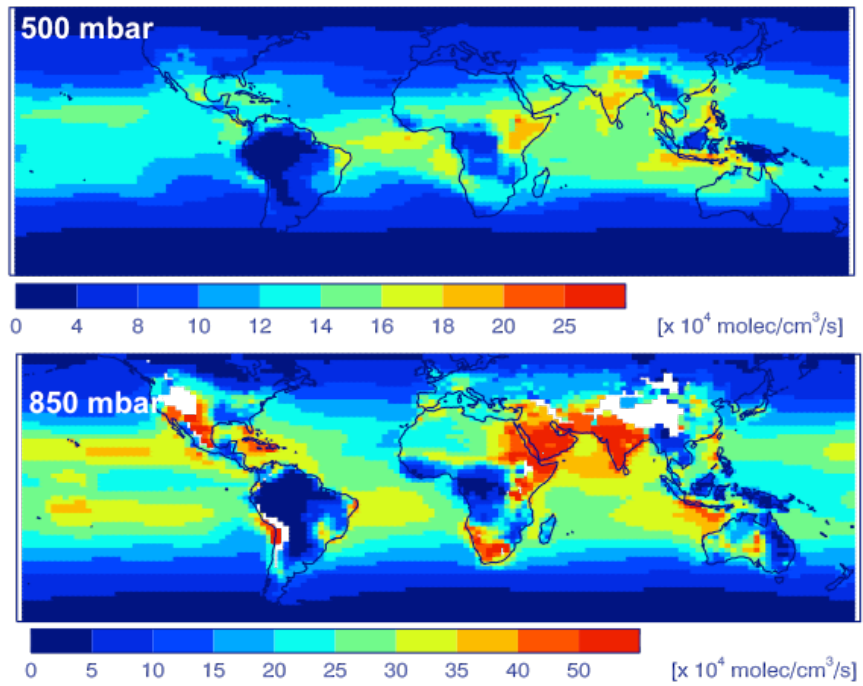
Fig. 18: Mean methane loss rate (1988-2007; x10^4 molecules/cm^3/s) at 500 mb (top) and 850 mb (bottom) for the *Base* scenario.
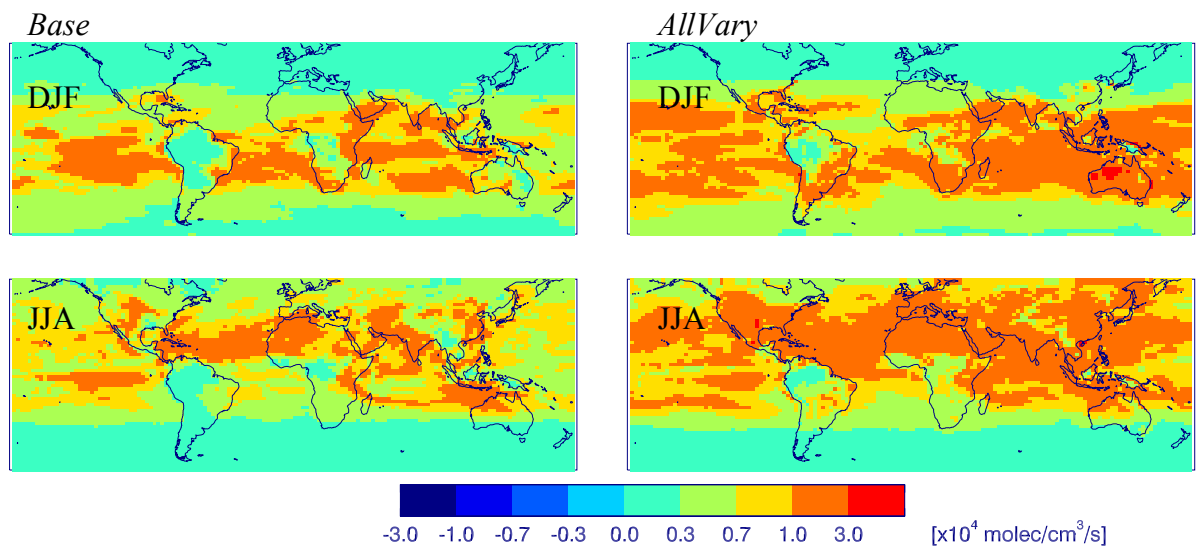
Fig. 19: Seasonal mean (1988-2007) standard deviation of tropospheric methane loss rates (x10^4 molecules/cm^3/s) from the *Base* (left column) and *AllVary* (right column) scenarios.
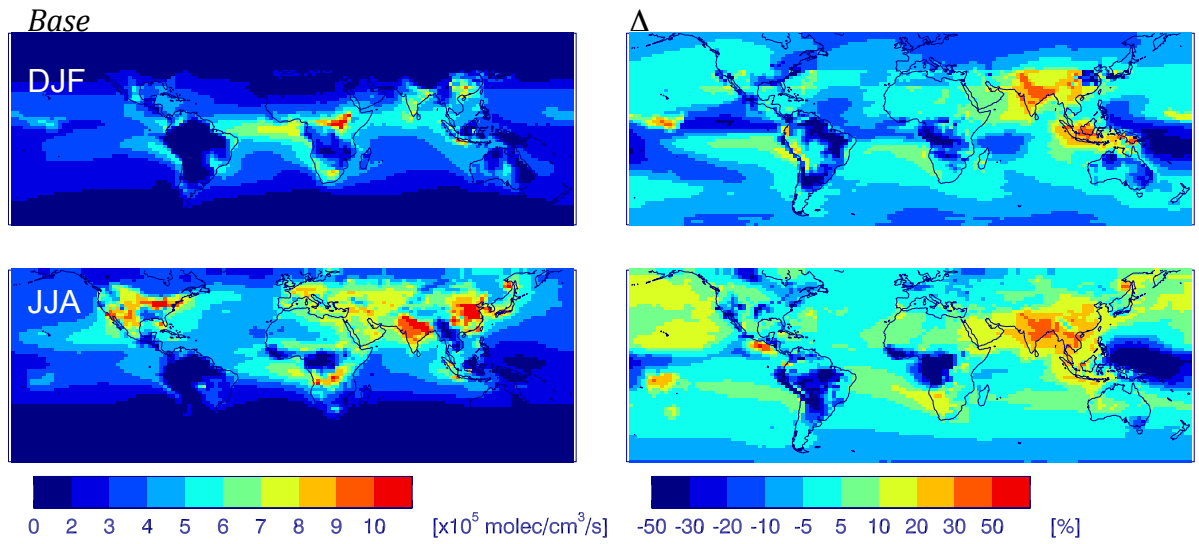
Fig. 20: Seasonal mean (1988-2007), mass-weighted tropospheric CO loss rates (left column; x10^5 molecules/cm^3/s) from the *Base* scenario and relative difference (%) between the *Base* and *AllVary* scenarios ((*Base-AllVary)/Base*; right column).
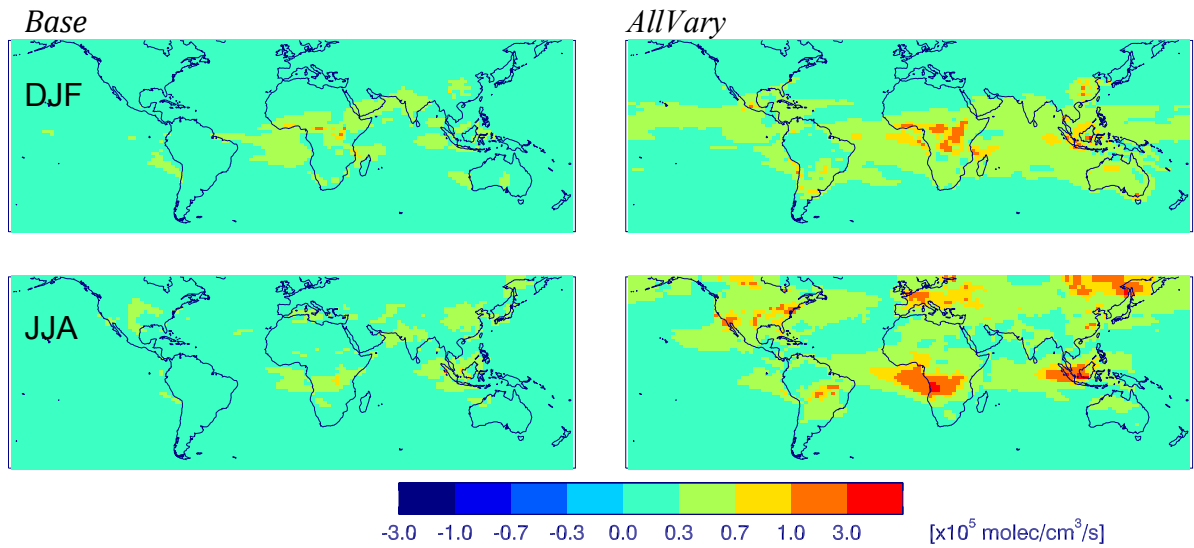
Fig. 21: Seasonal mean (1988-2007) standard deviation of tropospheric CO loss rates ($x10^5$ molecules/cm^3/s) from the *Base* (left column) and *AllVary* (right column) scenarios.
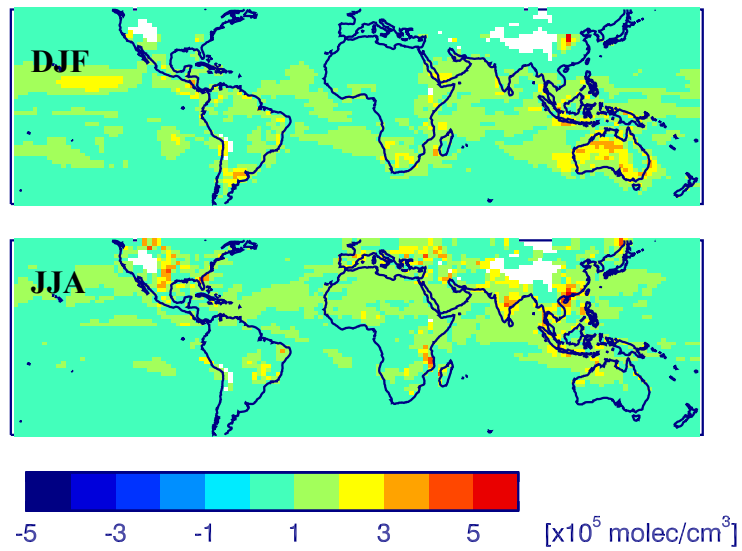
Fig. 22: Seasonal mean (1988-2007) standard deviations of OH (x10^5 molecules/cm^3) at 850 mb for the *AllVary* scenario.